DIPLOMARBEIT

Surface Science Studies of Hydroformylation on a Model Single-Atom Catalyst

ausgeführt am Institut für Angewandte Physik
der Technischen Universität Wien

unter der Anleitung von
Prof. Gareth S. Parkinson

durch

Manuel Ulreich

Matrikelnummer 01327673

Wien, 11. Dezember 2019

Manuel Ulreich	Gareth Parkinson

Acknowledgments

Gareth S. Parkinson for the opportunity for this thesis, as well as frequent visits to the lab for discussing experiments and results.

Zdeněk Jakub for patient supervision in the lab, valuable feedback on the entire thesis, and the STM data.

Jiří Pavelec for answering all my questions related to the TPD chamber.

Anna Niggas for reading my thesis and giving me feedback from a perspective outside of the surface science field.

Florian Kraushofer for feedback on my "Kurzfassung" and some details of the thesis.

Matthias Meier for the preliminary DFT calculations as well as detailed discussions about possible surface interactions.

Abstract

Catalysis is a highly relevant field in the chemical industry. Two groups into which catalysts can be divided are homogeneous and heterogeneous catalysts. Homogeneous catalysts typically are more efficient and selective compared to heterogeneous catalysts, but are also more difficult to separate from the products, and more expensive.

"Single-atom" catalysts are bound to a solid support, and thus belong to the heterogeneous group, yet are intended to bridge this gap, increasing selectivity and efficiency, while reducing the mass of the involved catalyst and therefore also the price. Hydroformylation (alkene + CO + H_2 $\rightarrow$ aldehyde) is an important industrial reaction typically performed in solution using highly-selective mononuclear complexes (i.e. homogeneously). Recently, rhodium-based "single-atom" catalysts have been shown to catalyze this reaction heterogeneously with similar levels of selectivity, suggesting single-atom catalysis can be a strategy to heterogenize problematic reactions.

In this work, surface science methods such as temperature-programmed desorption and X-ray photoelectron spectroscopy are used to study the critical component of coadsorption of C_2H_4 and CO on isolated rhodium adatoms on the $Fe_3O_4(001)$ surface, in context of hydroformylation. Reference data of C_2H_4 on the clean surface are also gathered. The results indicate that a monolayer coverage of C_2H_4 is equal to four molecules per unit cell. This is likely due to the four octahedrally coordinated iron atoms on the surface of the unit cell serving as adsorption sites. The data also show that 2-fold coordinated rhodium adatoms on the $Fe_3O_4(001)$ surface do coadsorb C_2H_4 and CO. Simultaneously they also show that the 5-fold coordinated rhodium adatoms incorporated in the surface layer do not adsorb C_2H_4. In conclusion, a method exists to manipulate the active site geometry such that coadsorption is possible, a vital step towards hydroformylation. Gaining control of the active site geometry is key to the development of highly-selective single-atom catalysis.

Kurzfassung

Katalyse is ein hoch relevantes Feld in der chemischen Industrie. Katalysatoren lassen sich in zwei Gruppen unterteilen, nämlich homogene und heterogene Katalysatoren. Homogene Katalysatoren sind typischerweise effizienter und selektiver im Vergleich zu heterogenen Katalysatoren, allerdings sind sie teurer, und es ist schwieriger sie von den Produkten zu separieren. Das Gegenteil trifft im Falle der heterogenen Katalyse zu.

Monoatomare Katalysatoren sind Teil der heterogenen Gruppe, haben allerdings das Potential dazu, die Vorteile der beiden Arten zu vereinen. Es soll dabei die Selektivität und Effizienz erhöht und die involvierte Masse des Katalysators sowie der Preis verringert werden. Hydroformylation (Alkene + CO + H_2 → Aldehyde) ist eine wichtige Reaktion, die in der Industrie typischerweise in einer Lösung mit hoch selektiven mononuklearen Komplexen (also homogen) katalysiert wird. Unlängst stellte sich heraus, dass rhodiumbasierte "monatomare" Katalysatoren diese Reaktion heterogen, allerdings mit ähnlicher Selektivität wie im homogenen Fall, katalysieren können. Das macht es plausibel, dass monoatomare Katalysatoren problematische Reaktionen heterogenisieren könnten.

In dieser Arbeit werden Methoden aus der Oberflächenphysik wie temperaturprogrammierte Desorption und Röntgenphotoelektronenspektroskopie verwendet, um den kritischen Schritt der Koadsorption von C_2H_4 und CO auf vereinzelt auf $Fe_3O_4(001)$ verteilten Rhodiumatomen im Kontext der Hydroformylation zu studieren. Die resultierenden Daten zeigen, dass die zweifach koordinierten Rhodiumadatome auf $Fe_3O_4(001)$ sehr wohl C_2H_4 und CO koadsorbieren. Gleichzeitig wird das Gegenteil für die fünffach koordinierten Rhodiumadatome gezeigt. Ebenfalls beweisen die Daten, dass es eine Methode gibt, die Koordination der Adatome beziehungsweise die Geometrie der Katalysestelle so zu beeinflussen, dass die Koadsorption ermöglicht wird. Die Kontrolle der Geometrie der Katalysestelle ist daher ein Schlüsselaspekt zur Entwicklung von hoch selektiven monoatomaren Katalysatoren.

Contents

1 Introduction

1.1 Single-atom Catalysis (SAC)

Catalysts are substances that increase the rate of a reaction. Two groups into which catalysts can be divided are homogeneous and heterogeneous catalysts[1]. Homogeneous catalysis occurs when the reactants are in the same phase as the catalyst. Heterogeneous catalysis is the alternative, in which case catalysis occurs at the interface of the reactants and the catalyst, which are in different phases. Homogeneous catalysis typically occurs in the liquid phase. Even though heterogeneous catalysis can take place in a liquid medium, the reactants are often gaseous while the catalyst is in the solid phase. On one hand, homogeneous catalysts are more efficient and selective. On the other hand, heterogeneous catalysts are more easily separated from the products, and are cheaper.

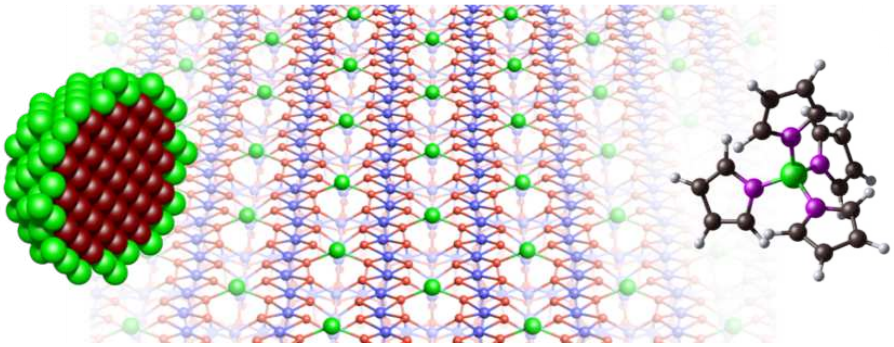

Figure 1.1: Heterogeneous nanoparticle catalysts (left) are active on the surface of the nanoparticle, containing effectively useless catalytic material in the core. Single-atom catalysts can be supported on different substrates in specific sites (center), and reduce the expensive catalytic material involved, but ideally also show similarly high selectivity and efficiency of homogeneous, mononuclear catalysts (right).

Single-atom catalysts (SACs) belong to the group of heterogeneous catalysts. Primarily, they reduce the catalytic material involved in heterogeneous catalysis. However, they also ideally maintain the selectivity and efficiency of soluble catalysts, while minimizing their disadvantages such as corrosion, and difficulty of separation from the

[1]The definitions of homogenous and heterogeneous catalysis are paraphrased from the IUPAC *Compendium of Chemical Terminology* [1].

products [2, 3]. Note that the selectivity depends upon the uniformity of the active site geometry [2]. As such, SACs can bridge the gap between homogeneous and heterogeneous catalysis [4–6]. Platinum, for example, is a rare and expensive noble-metal. It has been shown to work as a SAC for CO oxidation on iron-oxide nanocrystallites [7]. True to its name, SAC revolves around use of individual atoms for catalysis, effectively pushing the downsizing of supported-nanoparticle catalysis to the limit.

Downsizing of catalytically active nanoparticles has the benefit of reducing the involved mass of the catalyst, maximizing efficiency, and per-atom activity [8, 9]. In parallel, the issue of thermodynamical stability can arise, resulting in undesired clustering and sintering of adatoms [10]. Attempts to describe the nanoparticles stability as a function of radius, using the chemical potential μ, and the adhesion energy to the surface, exist [11]. To combat such phenomena, specific sites are engineered into support surfaces to reintroduce thermal stability to the system, for example by galvanic replacement, or sputtering, and atomic-layer deposition [12–14]. The concept is depicted in figure 1.2. In the case of $Fe_3O_4(001)$ it will be shown in section 1.4, that such a specific site for adsorption of adatoms is already part of the surface reconstruction.

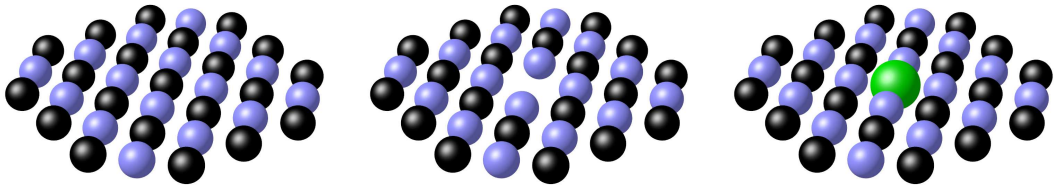

(a) Clean surface (b) Prepared vacancy (c) SAC site

Figure 1.2: The concept of preparing specific sites for stabilization of single atoms is illustrated. Titanium carbide is depicted as a substrate, but the process applies to substrates for SAC in general.

Apart from thermal instability, another issue emerges due to downsizing of the nanoclusters. Namely, the properties of these single atoms do not scale from their nanoparticle counterparts in a trivial manner [4, 15]. This makes sense from a physical point of view: interaction of small clusters, and especially single atoms, belong in a quantum mechanical domain [16, 17]. In other words, human intuition is not ideal for predicting changes in electronic structure, let alone their effects on these quantum mechanical systems. The trouble in observing and understanding such SAC systems, in part, lies in this quantum mechanical nature.

A typical in-situ SAC study involves synthesis of the powder catalyst, which is introduced into a reactor chamber to perform the reaction. The reaction is analyzed

in terms of the turnover frequency, and infrared absorption spectroscopy in which absorption patterns for specific bonds can be observed. Interpretation is often difficult, and identification of specific catalytic sites can be problematic. In contrast, in ultra-high vacuum (UHV) studies on model substrates a plethora of techniques is available to aid in this pursuit. Examples on the experimental side are scanning tunneling microscopy, atomic force microscopy, x-ray photoelectron spectroscopy, and temperature programmed desorption, to name a few. Density functional theory is the main technique employed for modeling on the theoretical side, as the systems being modeled tend to be large and therefore computationally intensive.

1.2 Hydroformylation

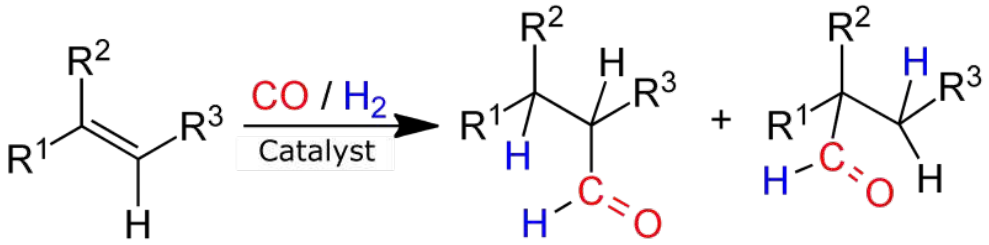

Figure 1.3: In the process of hydroformylation an alkene is transformed into an aldehyde with the help of CO, H_2, and a catalyst. Selectivity is an important issue in context of the choice of catalyst [18]. R^1 to R^3 are symbolic for organyl groups, or hydrogen.

Hydroformylation is the process of forming aldehydes from alkenes with the aid of carbon monoxide, hydrogen, and a catalyst. It is also known as the "oxo process". A general schematic of the process can be seen in figure 1.3. Aldehydes are then used for creation of esters, alcohols, and amines [18]. It "is one of the most important reactions for the manufacture of building blocks for the chemical industry" [19].

"Hydroformylation was discovered accidently [sic] in 1938 by Otto Roelen (1897-1993), (...) Today, the transformation represents one of the largest homogeneously catalyzed reactions in industry. The year 2008 saw the production of nearly 10.4 million metric tons of oxo chemicals[3]."

From Franke et al. [18].

Typical catalysts, in order of activity, are rhodium, cobalt, iridium, ruthenium, osmium, platinum, palladium, iron, and nickel [20]. Only rhodium and cobalt are used in industry, due to differences in activity of multiple orders of magnitude [19]. Hydroformylation is homogeneously catalyzed in solution, therefore requiring removal of the catalyst from the products [18]. This is one of the crucial disadvantages of homogeneous catalysis in general, and in the case of industrial hydroformylation even induces annual losses in the range of millions of euros at a typical 400 kt/year plant, if even one ppm of rhodium is lost per kg of product due to unsatisfactory recycling [21].

In contrast, heterogeneous catalysis would involve a catalyst in a different phase than the reactants and products, simplifying the entire process. Additionally, for all alkenes except ethylene the process results in some ratio of isomeric products [18]. This raises the important question of how to influence selectivity and choose the optimal catalyst. Answering this question requires comprehension of the hydroformylation process on a fundamental, atomic level. Ideally this understanding would lead to maximally efficient, heterogeneous usage of catalysts, in other words, single-atom catalysis.

1.3 Ethylene (C_2H_4)

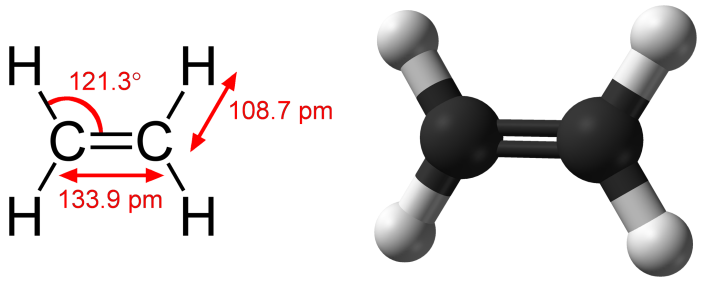

Figure 1.4: A structural formula (left) and a ball-and-stick model of ethylene are depicted.

Ethene, also known as ethylene, is the simplest molecule in the group of alkenes. The alkenes, sometimes also referred to as the olefins, are a group of unsaturated hydrocarbons characterized by the presence of a double bond between two carbon atoms. Ethylene's structure can be seen in figure 1.4. Due to its simplicity ethylene lends itself well as a candidate for the investigation of hydroformylation. That, and the fact that it has a boiling point approximately equal to 169 K, meaning it is gaseous at room temperature [22]. The hydroformylation of ethylene to propanal is portrayed in figure 1.5.

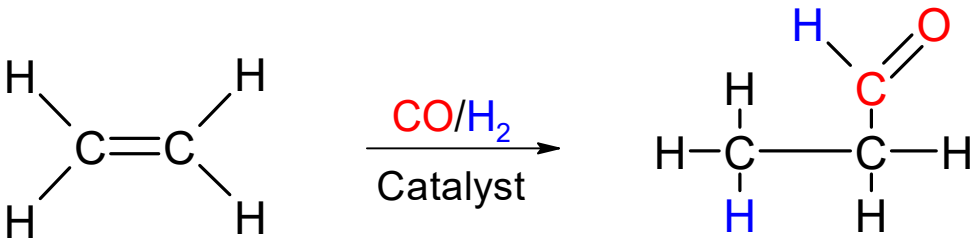

Figure 1.5: In the process of hydroformylation of ethylene the double c-c bond is broken, and a hydrogen is added as well as a formyl group. Angles and bond lengths are not to scale.

1.4 $Fe_3O_4(001)$

Consisting of iron and oxygen, the iron oxides are some of the most abundant materials on earth. While they are heavily involved in the worlds steel economies due to the iron component, among other things, they are also desirable for catalytic processes [23, 24]. More specifically, iron oxide-based catalysts are used in Fischer-Tropsch synthesis, the Fenton reaction, ethylbenzene dehydrogenation, and the water-gas shift reaction [25–28]. Magnetite is one of the many types of iron oxides.

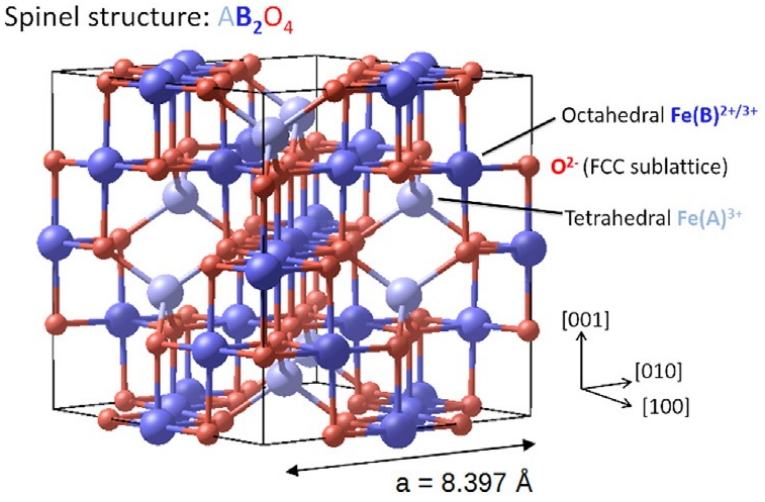

Figure 1.6: The bulk unit cell of magnetite (Fe_3O_4) is depicted. The species A and B refer to differently coordinated iron atoms. Adapted from Parkinson [23].

Magnetite is identified by the chemical formula Fe_3O_4, and has an inverse spinel structure, as seen in figure 1.6. It has a lattice constant of 8.397 Å. Considering the possible oxidation states of iron and oxygen, it is reasonable that Fe_3O_4 contains a

mixture of the iron cations Fe^{2+} and Fe^{3+} to reach an electrically neutral state while residing in a lattice of O^{2-} anions [23]. Fe_3O_4 has both tetrahedrally, as well as octahedrally coordinated iron atoms (Fe_{tet}, Fe_{oct}) in its unit cell. Alternating layers of Fe_{tet} and $(Fe_{oct})_2O_4$ form Fe_3O_4 in the (001) direction [29]. The Fe_3O_4(001) termination is of most relevance to this thesis, as it is the one used for all experiments.

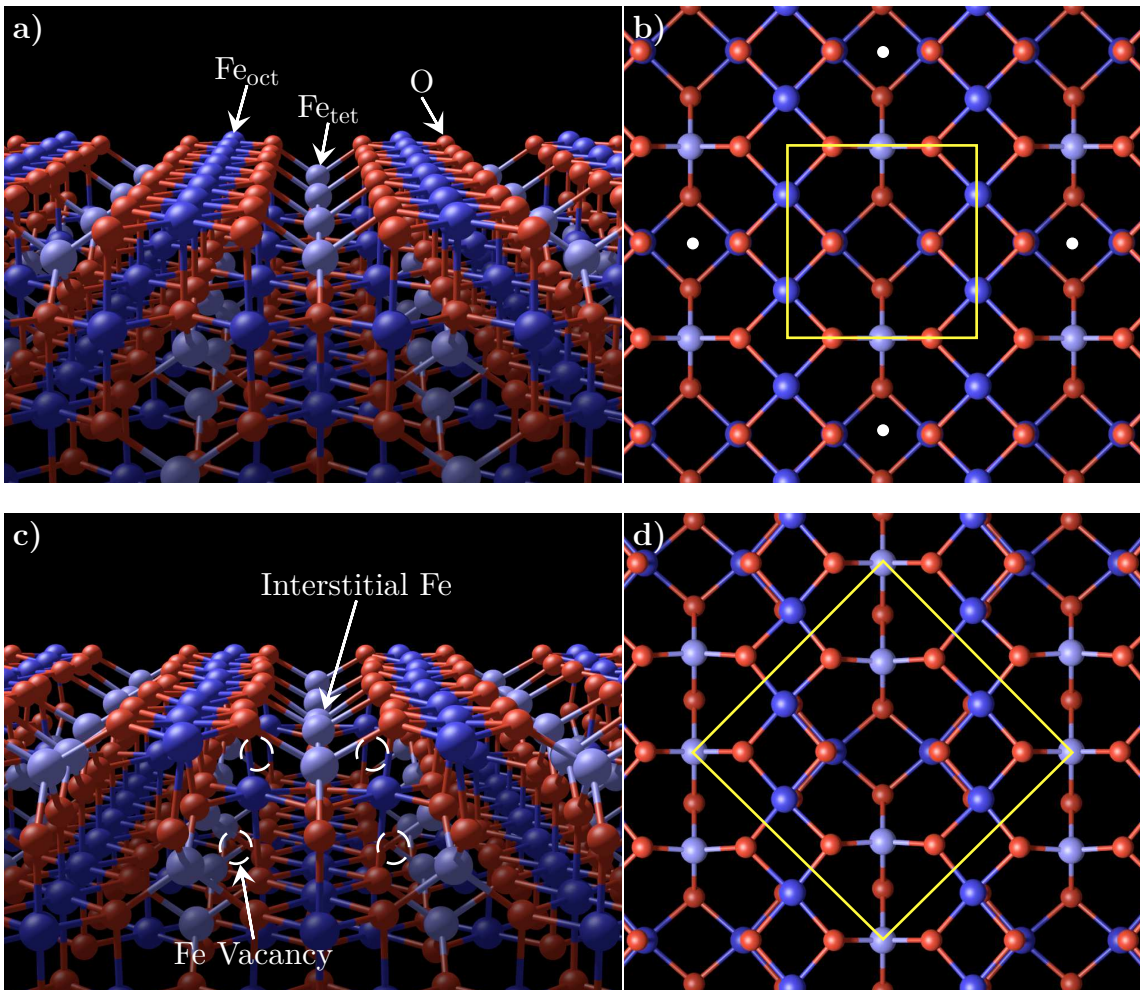

Figure 1.7: Both a bulk-truncated (top) and reconstructed (bottom) Fe_3O_4(001) surface are rendered [29]. Oxygen atoms are red, Fe_{tet} are light blue, and Fe_{oct} dark blue. On the left, perspective side projections are depicted. White dots in b) mark positions where iron interstitials will be placed. Orthogonal projection renders from the top are depicted in b) and d), with the yellow border marking the unit cell. The corners of the reconstructed unit cell mark the iron interstitials.

Hence, it is advantageous that the (001) termination simultaneously is one of the most stable, and best characterized variants of the magnetite facets. Over a wide range of chemical potentials, the most stable reconstruction is a $(\sqrt{2} \times \sqrt{2})$R45° reconstruction

with subsurface Fe_{oct} vacancies and an additional iron interstitial on the surface as seen in figure 1.7 [29, 30]. In the figure, the oxygen atoms are depicted in red, while Fe_{tet} is marked light blue, and Fe_{oct} blue. The reconstructed surface is illustrated on the bottom of the figure, with a perspective projection from the side in c) and an orthogonal projection from the top in d). The yellow boxes mark the respective unit cells. The unreconstructed counterparts can be observed in a) and b). The transition from the unreconstructed to the reconstructed surface involves adding an Fe_{tet} interstitial (seen in the center of c)) into every second oxygen bridge site, and removing two Fe_{oct} atoms in the subsurface (missing blue atoms in the vicinity of the interstital Fe_{tet} in c)). The remaining oxygen bridge site in the center of the unit cell is the preferred adsorption site for adatoms, as shown by Bliem et. al [29].

Since the adsorption of 2-fold and 5-fold coordinated rhodium will become relevant in the results section, the two sites are depicted in figure 1.8. On the top, in a) and b), the 2-fold coordinated rhodium site is portrayed. This rhodium site can be prepared by depositing sub-monolayer coverages of rhodium (less than one atom per unit cell) at 300 K [30, 31]. On the left, in a), a rendered image of a rhodium adatom in the oxygen bridge site can be observed. On the right, in b), an image taken via scanning-tunneling microscopy (STM) is depicted. The iron rows (dark blue in the rendered images) are overlayed with white arrows. The rhodium atom sits between the parallel iron rows, as in the rendered image. On the bottom, in c) and d), similar images are displayed for the 5-fold coordinated rhodium site. This site can be prepared by dosing rhodium at 300 K and then annealing to 420 K for a few minutes [30, 31]. On the left, in c), the rendered image shows the rhodium adatom incorporated into the surface, in place of an Fe_{oct}. On the right, in d), a STM image corresponding to the 5-fold rhodium site is shown. The white arrows highlight the iron rows as before, but in contrast to b), the rhodium atom sits on top of an iron row (in the path of an arrow). At temperatures beyond 420 K the rhodium starts diffusing to the bulk material. If a comprehensive, more in-depth pool of knowledge of the iron oxides is desired, the review written by G. S. Parkinson is suggested as a reference [23].

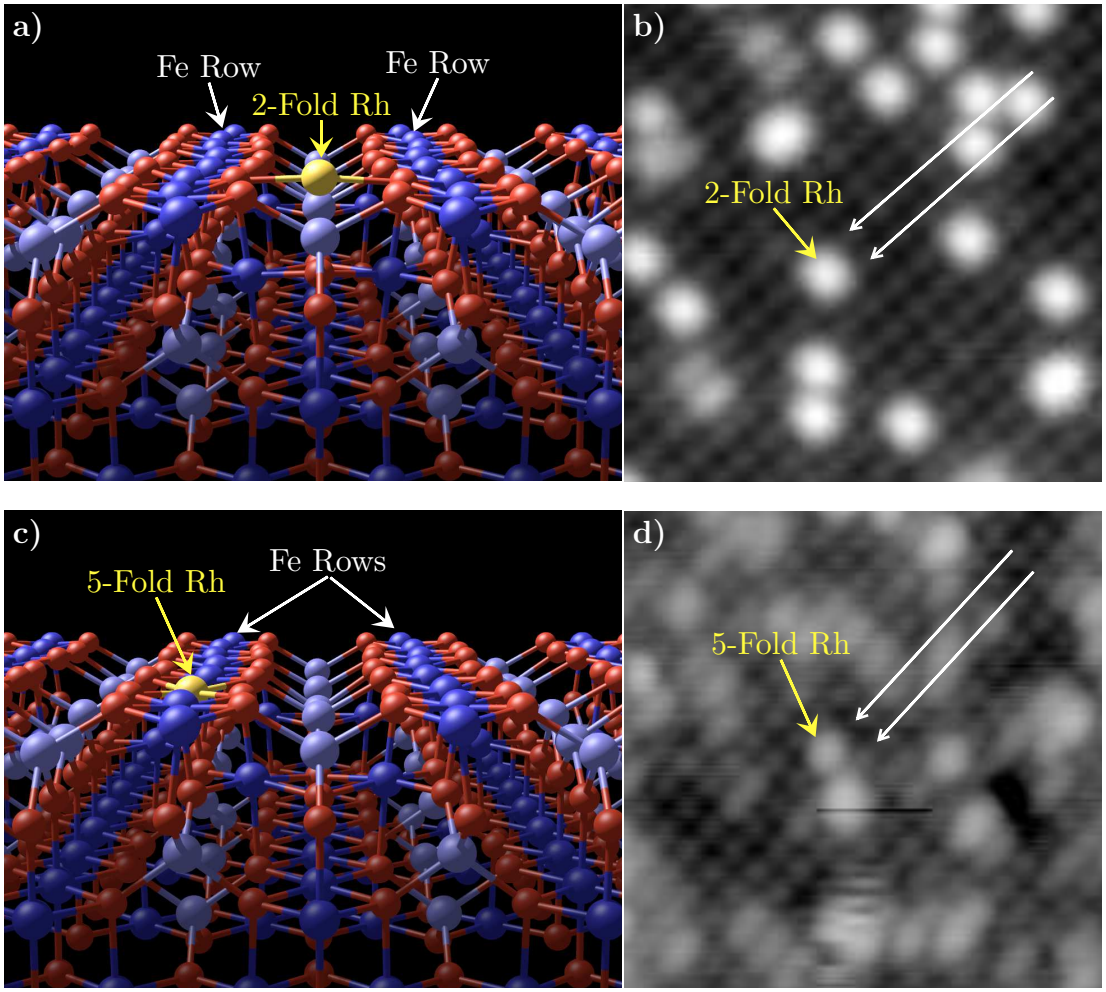

Figure 1.8: A render of the $Fe_3O_4(001)$ surface with a 2-fold coordinated rhodium adatom in the preferred adsorption site is shown in a). The corresponding scanning-tunneling microscopy (STM) image is depicted in b). White arrows are overlayed over the iron rows. In c) and d) the same scenarios are illustrated for a 5-fold coordinated rhodium adatom.

2 Experimental Methods

2.1 Temperature-programmed Desorption (TPD)

One of the two main techniques employed over the course of this thesis is temperature-programmed desorption. Concisely stated, it involves deposition of a substance onto the sample, followed by desorption via controlled heating of the sample. The desorption is analyzed with the aid of concurrent mass spectrometry. This produces a spectrum of counts versus time for each tracked mass, which can be converted into a spectrum of counts (or desorption rate) versus sample temperature. The latter spectrum allows determining the desorption energy of a species, as well as desorption order.

Both the deposition of the desired species and the desorption process can be described in detail. Traditionally deposition involves backfilling the chamber with the desired gas. In this case, due to a custom-built molecular beam, deposition essentially reduces to firing a gaseous beam at the sample in a controlled fashion. The species originates from a gas bottle attached to an intermediate reservoir via a gas line with a leak valve. The reservoir leads to the molecular beam which is sealed by the beam gate. The effusive molecular beam is formed by expansion of the gas through two differentially pumped stages. Dosing the gas is equivalent to opening the beam gate. The sample is cryogenically cooled to a specific temperature to allow for adsorption of the molecules. The next step is desorption.

The desorption process is thermally driven, thus the name *temperature-programmed* desorption. An Arrhenius equation is used to describe the desorption rate. The mathematical model depends on a pre-exponential factor k_d, a desorption order m, and the desorption energy E_d, as seen in equation 2.1. N is the fractional coverage, and k_b the Boltzmann constant. T is the temperature.

$$\frac{\mathrm{d}N}{\mathrm{d}t} = -k_d N^m \exp\left(\frac{-E_d}{k_B T(t)}\right) \tag{2.1}$$

The temperature is described with starting temperature T_0 and the heating rate β.

$$T(t) = T_0 + \beta t \tag{2.2}$$

The sample is heated at a set rate, for example 1K/s, for a set time, while the mass

spectrometer records the counts for a specified set of masses, typically adapted to the cracking pattern of the expected species. As the sample plate is resistively heated, and the thermocouple is mounted to the sample plate, there is a temperature gradient between the surface of the sample, and the sample plate. This depends on heating rate, sample thickness, mounting pressure, and mounting method (with/without a gold foil, for example) introducing systematic error. While it would be preferable to remove this error entirely, one can minimize it by maximizing thermal conductivity, and using sufficiently low heating rates. Another possibility is to calibrate it on basis of known multilayer desorption temperatures of a specific substance. Since the error is of systematic nature, meaning it is present during all measurements and in a similar magnitude, it typically is sufficient to consider this error during data analysis. Due to the custom-built molecular beam, quantitative TPD analysis is possible with the setup used in this thesis. The analysis process is layed out in section 3.1 alongside the chamber specifics.

2.2 X-Ray Photoelectron Spectroscopy (XPS)

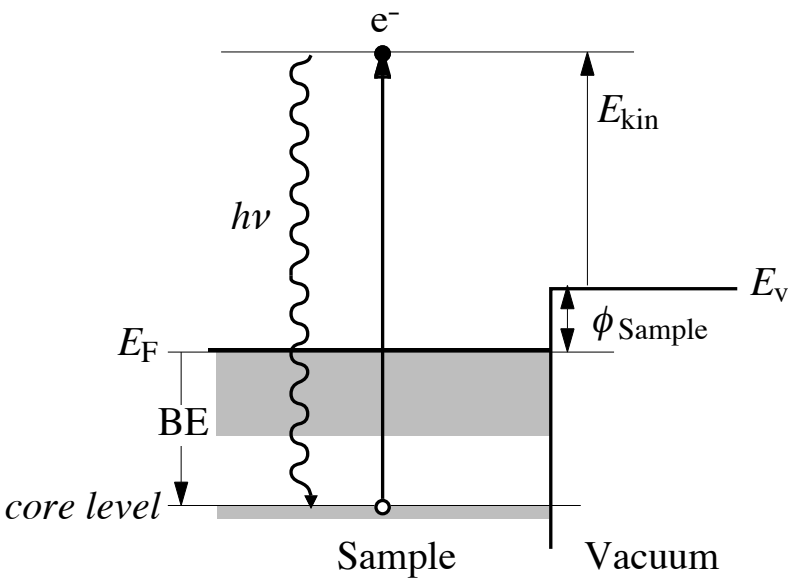

Figure 2.1: A single-electron process occuring during XPS is illustrated. An incoming photon with the energy $h\nu$ deposits its energy on an electron e^-. The electron is ejected from a core shell and the binding energy BE is "lost" leaving the electron with kinetic energy E_{kin}. This is in reference to the vacuum energy E_V. The difference between the Fermi-Energy E_F and E_V is equivalent to the work function ϕ of the sample. Image adapted from Schmid [32].

$$h\nu = E_{kin} + \phi_{sample} + E_{binding} \tag{2.3}$$

The second of two main techniques used within the span of this thesis is x-ray photoelectron spectroscopy. In short, the method entails shining an x-ray beam onto the sample, which results in photoelectron emission with a spectrum specific to the core-shells of the material, thus permitting unique identification of the elements. Equation 2.3 shows the relationship between the kinetic energy E_{kin} of the ejected electron and the energy of the incoming photon $h\nu$, assuming a single-electron process. ϕ_{sample} is the work-function of the sample. A visual representation of the single-electron process can be observed in figure 2.2.

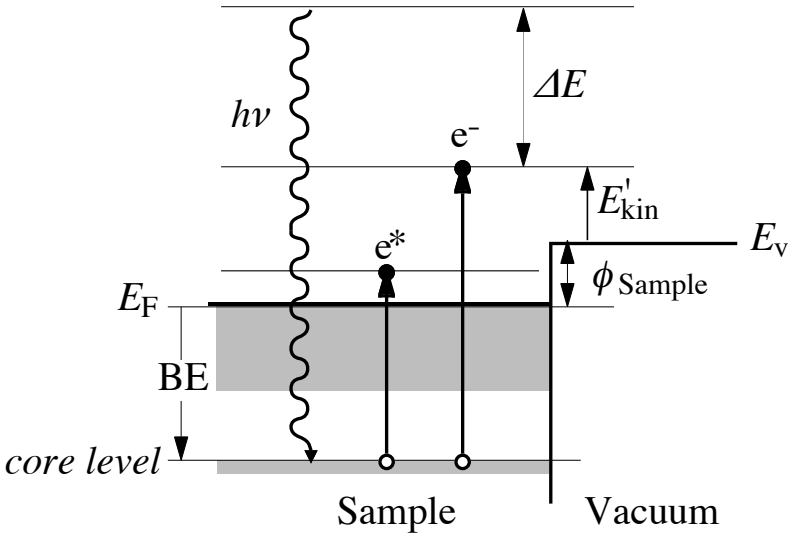

Figure 2.2: The shake-up process is depicted where an electron e^* is excited and the photoelectron e^- has lower kinetic energy E'_{kin} than in a single-electron process. The satellite peak is shifted by ΔE from the primary peak, which corresponds to the excitation energy of e^* (energies not to scale). The excited electron will decay eventually. Image adapted from Schmid [32].

Multi-electron processes are also possible, resulting in satellite peaks which are shifted by the energy lost to excitation of the other electron(s). Shake-up, and shake-off peaks are an example of such processes. During shake-up a fraction of the photon's energy $h\nu$ is used (by chance) for the excitation of a second electron e^*, thus reducing the energy of the photoelectron e^- by the same amount. The shake-off process is similar, except enough energy is passed on to the second electron, that it becomes a photoelectron itself. In both cases, satellite peaks emerge in the vicinity of the primary peaks. Chemical

shifts due to different chemical environments are another possibility. The XPS peaks of bulk material versus those of surface layers will also differ due to surface-core-level shifts. A visual representation of a shake-up process can be observed in figure 2.1.

The photoelectron distribution can be analyzed with a hemisperical analyzer. Under grazing emission angles, the technique becomes more surface-sensitive. For this reason, all XPS data is measured with grazing emission in this thesis. The resulting spectrum depicts counts versus kinetic or binding energy of the electron. In theory quantitative analysis is possible. In practice uncertainty attached to fitting multiple peaks per XPS peak is often too high to warrant quantification. Relative sensitivity factors of different elements add further complexity, requiring calibration with multiple samples whose chemical makeup is known precisely. Nonetheless the XPS spectra allow for observation of core-level shifts. This provides information about more trivial things such as the success of sample preparation, but also more complex phenomena such as binding of an adsorbate to a metal adatom, especially when combined with other techniques.

2.3 Ultraviolet Photoelectron Spectroscopy (UPS)

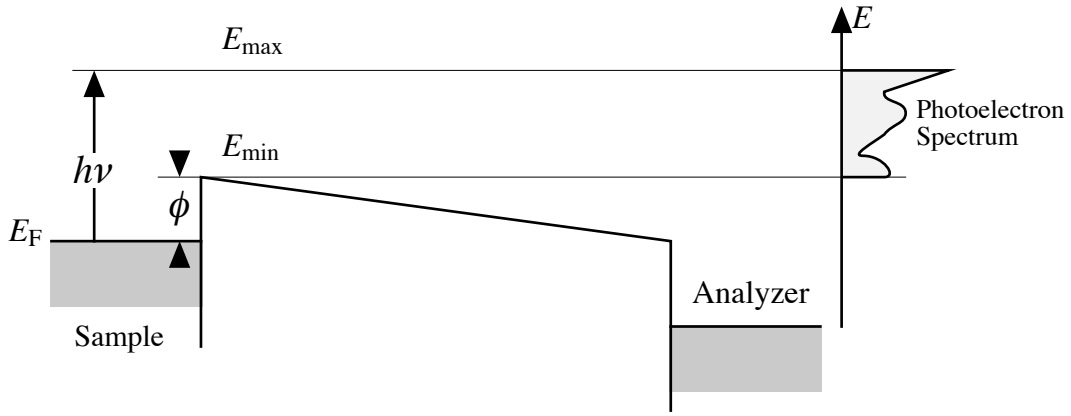

Figure 2.3: The concept of measuring the work-function with UPS is illustrated. The quantities $h\nu$, ϕ and E_F are the same as in previous XPS figures. E_{max} and E_{min} correspond to the highest and lowest kinetic energies photoelectrons can have for a given photon energy. Image adapted from Schmid [32].

UPS follows precisely the same principals as XPS, with the only difference being the wavelength of the incoming radiation. As the name of the technique says, it is in the ultraviolet spectrum. Thus, valence states near the Fermi edge are examined,

rather than core-level states. The same analyzer can be employed to gather data, however the X-Ray source is exchanged with a UV source. It is possible to measure the work-function of the sample, as illustrated in figure 2.3. Each photon used to probe the density of states (DOS) of the sample deposits the energy $h\nu$ in an electron. A part of this energy is used to overcome the work-function ϕ. Another fraction is used to overcome the binding energy. The remaining energy is the kinetic energy of the photoelectron. Thus the difference between the maximum and the minimum kinetic energies plus the work function has to be equal to the photon energy. This relationship is shown in equation 2.4. It can be used to solve for the work-function of the sample, since $h\nu$ and $E_{max} - E_{min}$ are known.

$$h\nu = E_{max} - E_{min} + \phi_{Sample} \tag{2.4}$$

3 Experimental Setup

3.1 The TPD Chamber

All experimental data were gathered within an ultra-high-vacuum (UHV) chamber. Due to its designated purpose it is named "TPD Chamber". Everything is centered around a rotary manipulator capable of translational x, y, z motion as well as rotational φ motion. The manipulator also houses a flow cryostat. Equipment typical for surface science techniques is positioned concentrically around the main chamber in which the manipulator resides.

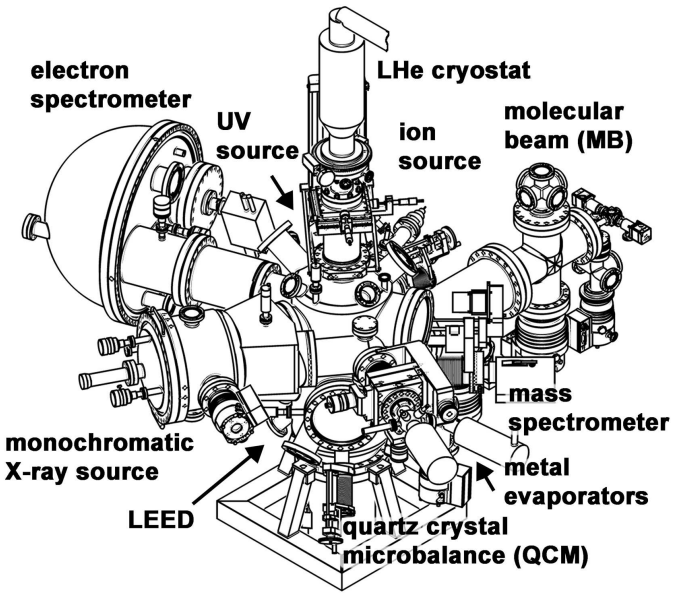

Figure 3.1: Chamber schematic adapted from Pavelec et. al [33].

This includes a monochromatic X-ray source, an ultraviolet source, a hemispherical analyzer, an ion source, multiple metal evaporators, a quartz crystal microbalance (QCM) and a low-energy electron diffraction (LEED) setup. The X-ray source has a silver and an aluminum anode. In the course of this thesis, all spectra were taken with the latter anode, an emission current of 27 mA and an acceleration voltage of 13 kV. The UV source functions on basis of an excited helium plasma, providing He-I (21.2 eV)

and He-II (40.8 eV) lines. Care was taken to minimize the He-II contribution for all UPS spectra. A combination of four roughing pumps and five turbo pumps maintain a base pressure of approximately 10^{-11} mbar in the main chamber. A schematic of the setup can is depicted in figure 3.1. The two most significant entities are the molecular beam, as well as the quadrupole mass spectrometer, both of which are integral to TPD.

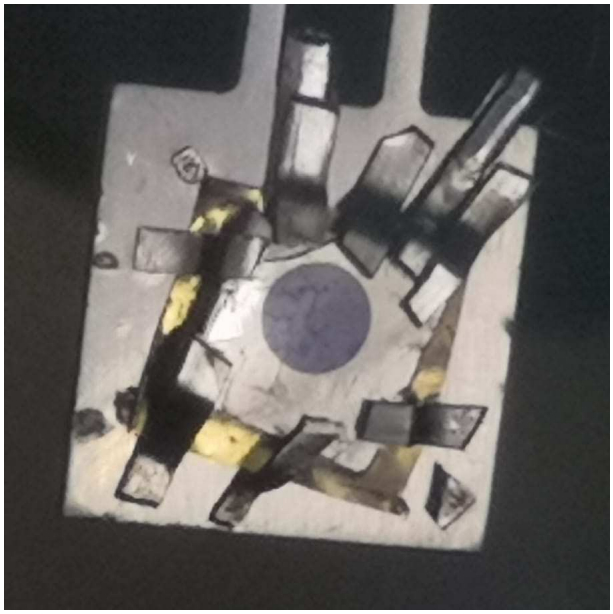

Figure 3.2: An overnight dose of D_2O is visible on the $Fe_3O_4(001)$sample. It is used to calibrate the dose rate via the spot diameter.

The molecular beam is custom-made[1] such that one can perform not just qualitative, but quantitative TPD [34]. This means one can determine how many molecules per unit cell are dosed per second or per Langmuir ($1\,\mathrm{L} = 10^{-6}\,\mathrm{Torr\,s}$). A prerequisite for this calculation is the beam spot diameter. This is determined by dosing water onto the sample overnight, which forms a spot of black ice whose diameter can be measured. Measurement is executed digitally with reference to the six mm sample side length. An image of such a spot is displayed in figure 3.2. Calculation of the dose rate is then performed as by Pavelec et al. [33]. The goal is to calculate the particle flow (collision rate) per unit cell onto the sample, as shown in equation 3.1.

$$J_{Sample} = \frac{p_{Beam}\tilde{v}_{Gas}}{4k_BT}A_{UC} \quad [J_{sample}] = \frac{\text{Particles}}{\text{Unit Cell} \cdot \text{Second}} \tag{3.1}$$

In the equation, p_{Beam} is the molecular beam pressure at the sample, $\tilde{v}_{Gas}$ is the average velocity of the gas molecules being dosed, k_B is the Boltzmann constant, T the

[1] D. Halwidl's masters thesis contains all details of the beam construction and the TPD chamber.

temperature, and A_{UC} the surface area of a unit cell in square meters. The average gas velocity $\tilde{v}_{Gas}$ is calculated for an ideal gas in equation 3.2, with the molar mass m (in g/mol).

$$\tilde{v}_{Gas} = \sqrt{\frac{8k_BT}{\pi m}} \tag{3.2}$$

Since the beam geometry is known, p_{Beam} can be calculated from the reservoir pressure, as performed in equation 3.3.

$$p_{Beam} = \frac{1}{4} p_{Res} \gamma(Kn_{Gas}) \frac{d_o^2}{L^2} \tag{3.3}$$

The reservoir pressure p_{Res} is measured in-situ (typically 0.533 mbar or 0.40 Torr), and the distance between the molecular beam orifice and the sample L can be determined with geometric relations from the previously measured beam spot diameter. The factor $\gamma(Kn_{Gas})$ corrects for gas viscosity, and has been calibrated as shown in the supplemental information of Pavelec et. al [33]. It is a function of the Knudsen number of the gas Kn_{Gas}. The distance L is determined in equation 3.4. The distance between the orifice and the exit aperture L_a (51.0 mm), as well as the aperture diameter d_a (2.0 mm), and the orifice diameter d_o (37.9 µm) are constants of the molecular beam geometry. d_s is the spot diameter.

$$L = L_a \frac{d_s}{d_a} \tag{3.4}$$

Since the same parameters are used dosing C_2H_4 in the course of the experiments, it is sufficient to determine the particle flow onto the sample surface once:

$$J_{C_2H_4} = 0.0624 \frac{C_2H_4}{\text{Unit Cell} \cdot \text{Second}} \approx 3.12 \frac{C_2H_4}{\text{Unit Cell} \cdot \text{Langmuir}} \tag{3.5}$$

Note that the sticking coefficient still needs to be determined after calculating J_{Sample}, since it is not given that all particles impinging on the sample also remain on the sample. The sticking coefficient measurement is described in the results subsection 4.1.2.

4 Results

4.1 Studies of C_2H_4 on $Fe_3O_4(001)$

When approaching a complicated process like hydroformylation, understanding clean surface chemistry is a prerequisite to understanding adatoms. In this case, that suggests analysis of C_2H_4 on $Fe_3O_4(001)$ with the help of TPD, XPS, and UPS.

4.1.1 Sample Preparation

First, a standard preparation process was determined for the clean $Fe_3O_4(001)$ surface, both with the help of literature and experimental data. The idea is to reproducibly provide a clean surface as a baseline for experiments. XPS data is used for judging the state of the surface.

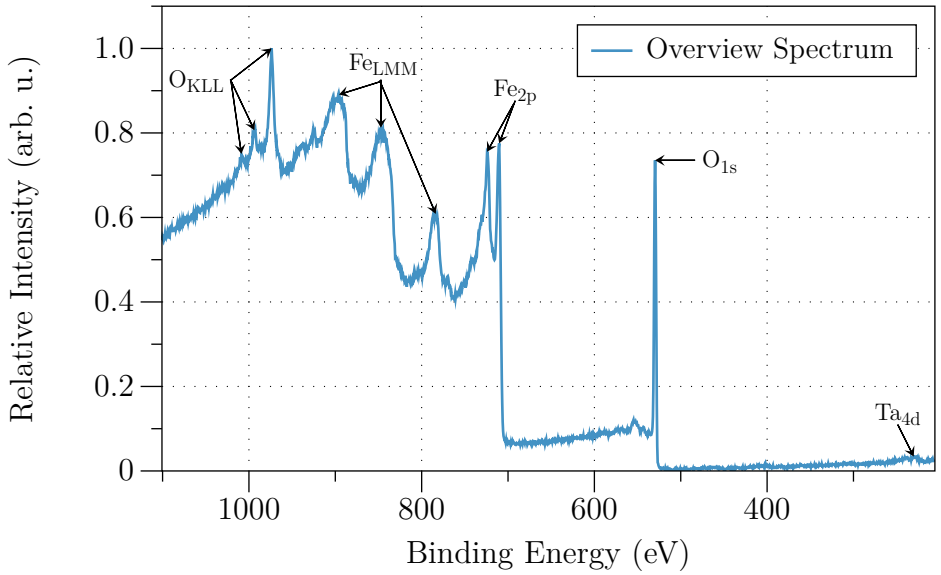

Figure 4.1: An overview spectrum of grazing-emission XPS after standard preparation is shown. Major Auger peaks and spectral lines are labeled. The tantalum signal originates from the mounting clips.

Two techniques are suitable for sample preparation: sputtering the surface with ions, and annealing at a high temperature. Sputtering disrupts the surface structure and removes atoms from the sample surface, effectively "cleaning" it. Annealing permits reordering of the atoms. At the same time, sputtering preferentially removes oxygen atoms from the surface. To counteract this effect, the annealing process is intermittently carried out in reoxidizing conditions.

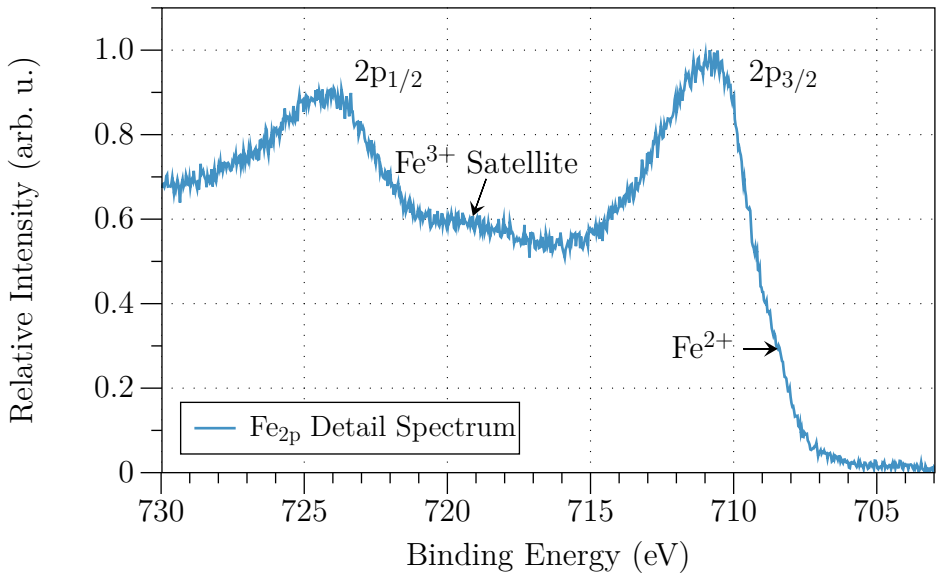

Figure 4.2: A high-resolution grazing-emission XPS spectrum of the Fe2p peaks after standard preparation is portrayed. The Fe^{2+} shoulder and Fe^{3+} shake-up features are also labeled [29, 35].

The number of cycles can differ slightly between preparations, as the state of the surface is judged by the XPS spectra. Preparation continues until the XPS spectra represent a clean surface. The XPS spectra are known to correspond to a specific surface preparation, on basis of previous research. In the dissertation of J. Hulva, which focuses on $Fe_3O_4(001)$, an annealing temperature of 950 K is suggested [31]. All intervals except reoxidation (30 min) and post-annealing (20 min) take 15 minutes. The reoxidation interval also differs from the annealing interval by an O_2 background pressure of 5×10^{-7} mbar.

XPS was performed at 300 K to check the sample surface after standard preparation. A grazing emission angle of $\theta = 75°$ was used for all XPS spectra for maximal surface sensitivity. An overview spectrum can be seen in figure 4.1. The Auger peaks of iron and oxygen are clearly visible, as well as their photoelectron lines. Additionally a minute amount of tantalum can be seen, indicating that the mounting clips are located slightly

within the measured area during spectroscopy. This makes sense, as grazing-emission XPS requires the sample to be tilted in a manner such that it is impossible to avoid measuring the mounting clips. High-resolution spectra of iron, oxygen, carbon, and rhodium peaks were acquired as well. Figure 4.2 shows the Fe2p peaks as well as two satellite peaks [35]. The satellite peaks are attributed[1] to Fe^{2+} and Fe^{3+} [29, 35]. The O1s peak is visible in figure 4.3 around 530 eV as expected for iron oxides [36].

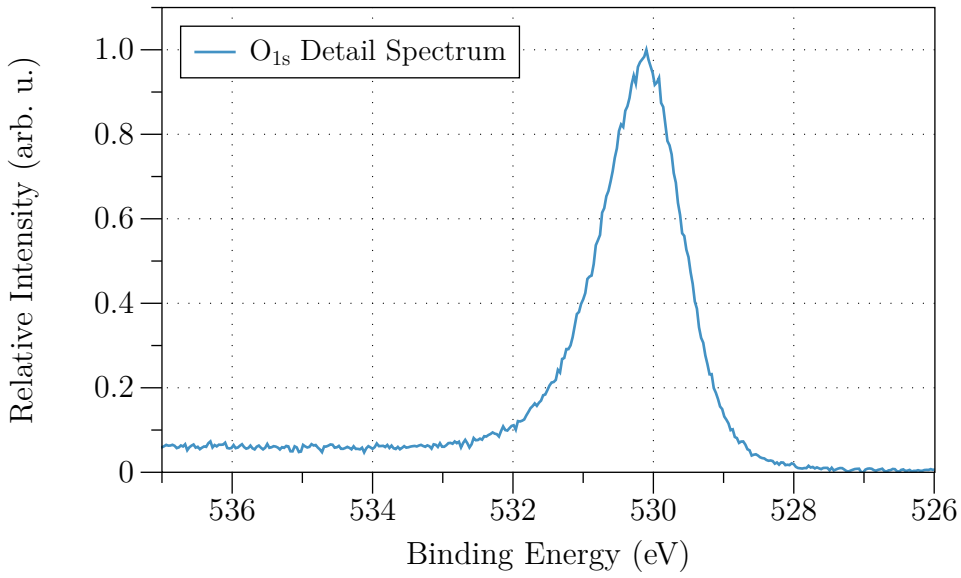

Figure 4.3: A high-resolution grazing-emission XPS spectrum of the O1s peak after standard preparation is depicted.

Spectra of the energy ranges in which the C1s and Rh3d peaks should be located were measured as well. They are shown in figure 4.4. The grey ranges indicate the expected position of the photoelectron peaks, as the magnified spectra are dominated by noise. This is intended however, as standard preparation should remove all carbon and rhodium from the surface of the sample. Arguably, a slight bulge around 307.5 eV could be attributed to the rhodium $3d_{5/2}$ peak. It should be noted, that this spectrum was taken toward the end of the series of experiments, after many rhodium depositions and even more cleaning cycles. The signal does not decrease with multiple standard preparation cycles. This suggests that the rhodium is located on the side of the mounting clips, which are barely sputtered during standard preparation, but are definitely located inside the X-ray spot during grazing-emission XPS. Importantly, the C1s peak is indisputably absent, signifying removal of carbon-based species, within the sensitivity

[1] In the supplementary material, in the case of Bliem et. al.

of the analyzer. C_2H_4 TPDs were performed to confirm absence of rhodium.[2] While there may be rhodium somewhere on the sample plate or the clips, the area targeted by the molecular beam was free of rhodium.

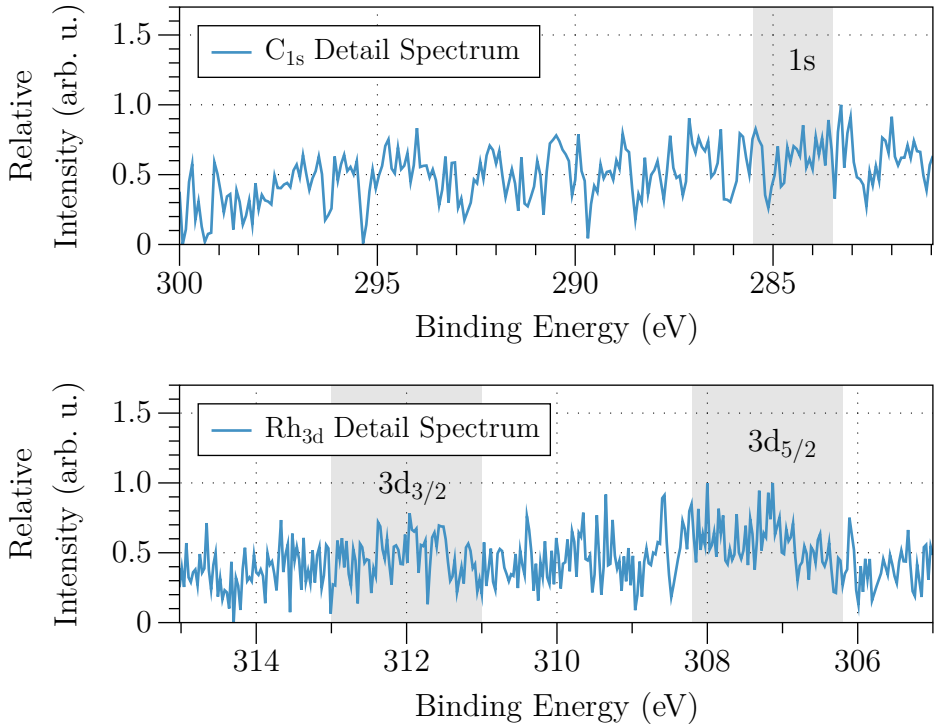

Figure 4.4: High-resolution grazing-emission XPS spectra of the C1s (top) and Rh3d (bottom) regions after standard preparation are shown. The area in which the respective peaks would be expected are highlighted. As intended, standard preparation cleans the surface and leaves no carbon or rhodium behind.

4.1.2 Sticking Coefficient Measurement

In order to relate the dose in Langmuir to an equivalent monolayer coverage in molecules per unit cell, it is necessary to determine the sticking coefficient. This coefficient represents what fraction of the molecules fired at the sample surface also remains on the sample surface. Determining the sticking coefficient effectively only requires firing the molecular beam at the sample at two different temperatures and recording the counts over time (or dose). The higher temperatures needs to guarantee reflection of all molecules off the sample. The lower temperature is the one at which the sticking

[2]The high temperature rhodium peak is unique and would immediately be visible if there were any rhodium left. This was never the case. See section 4.1.6.

coefficient should be measured. The measurement is portrayed in figure 4.5. Calculating the sticking coefficient then reduces to dividing the number of counts at the higher temperature (complete reflection) by the number of counts at the lower temperature (partial to no reflection).

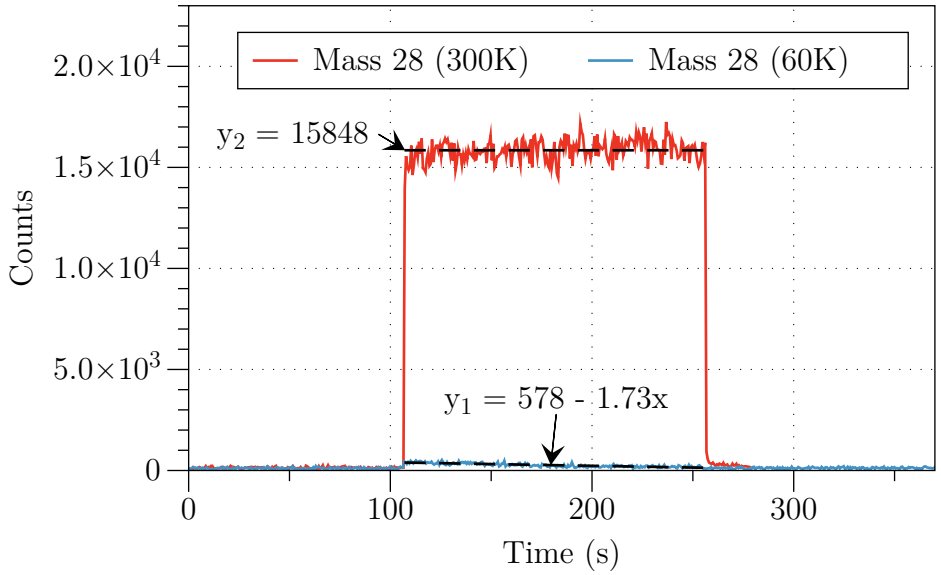

Figure 4.5: The sticking coefficient measurement of C_2H_4 at 60 K is shown. The figure shows that it starts at 97.5% and increases to 100% after 150 seconds (3L).

4.1.3 Data of C_2H_4 on the Clean Fe_3O_4(001) Surface

The first series of experiments is performed on the clean surface. Various coverages of C_2H_4 are dosed onto the surface at a sample temperature of 60 K, and then investigated with TPD, XPS, and UPS. Figure 4.6 displays an overview of the TPD series. Doses from 0.30-9.24 molecules per unit cell (M/UC) are depicted. Each TPD spectrum was configured to begin at 60 K and end at 680 K with a temperature ramp of 1 K/s. The spectra were measured back to back, but in random order, with the help of an autopilot feature in the control software. The autopilot mode allows for highly consistent TPD series, especially when compared to manual execution. The dominant feature in the depicted TPD series is the multilayer peak visible from 4.13 M/UC upwards. The magnified region shows two peaks associated with multilayer coverages between 1.35 L and 2.40 L, which merge into a single peak above a dose of 2.40 L. Nonetheless, the multilayer behavior of C_2H_4 is not as relevant as the (sub) monolayer behavior, as further experiments will be conducted with coverages below one monolayer (ML).

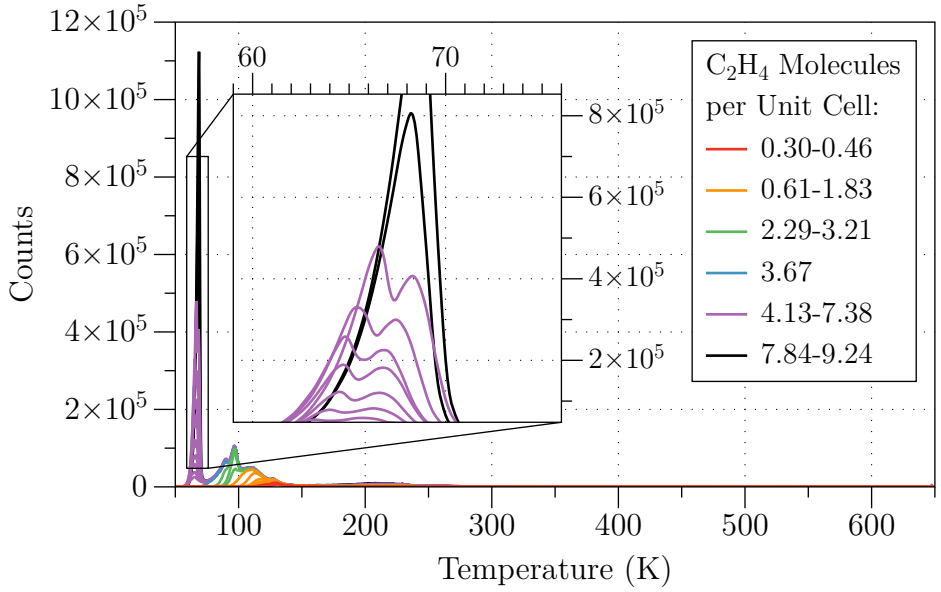

Figure 4.6: Overview of the TPD series from 0.30-9.24 C_2H_4 molecules per $Fe_3O_4(001)$ unit cell (0.10-3.00 L). The dual multilayer peak is magnified. The two peaks merge above a coverage of 7.38 C_2H_4 per unit cell. For each spectrum, the sample was cooled to 60 K, then C_2H_4 was dosed, and then heated at 1 K/s to 680 K.

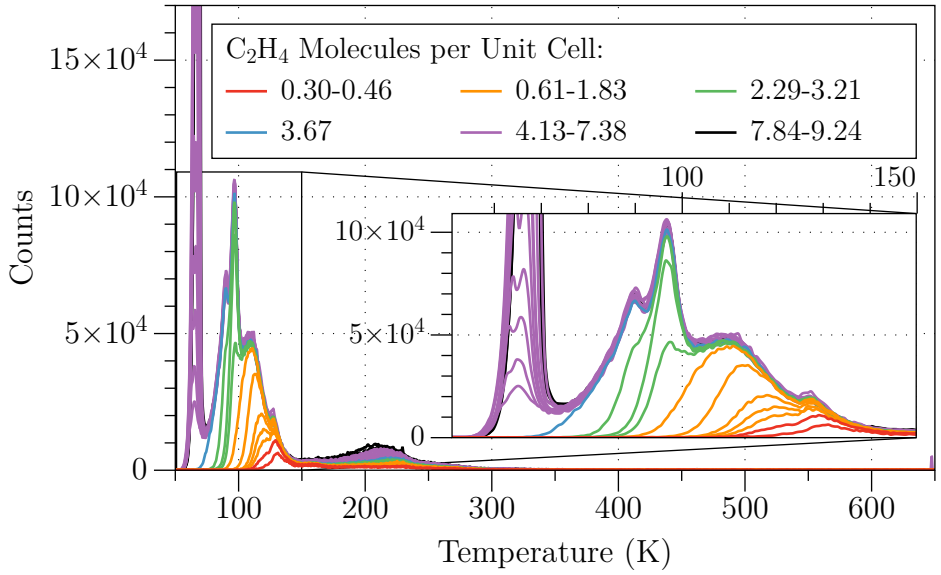

Figure 4.7: A closeup view of the TPD series is portrayed. The spectrum closest to showing a multilayer peak has a coverage of 3.67 C_2H_4 per unit cell. Since the $Fe_3O_4(001)$ unit cell surface has four Fe_{oct}, likely acting as adsorption sites, the monolayer coverage probably equates to 4 C_2H_4 per unit cell. One can identify five individual peaks for the monolayer. Additionally the unusual peak for multilayer coverages can be observed.

The TPD features at and below 4 M/UC are recognizable in the overview spectrum, but additional magnification is necessary. Figure 4.7 cuts off the multilayer peak, but provides an enlarged view of the smaller features. One can identify four peaks between 80 K and 130 K, and a fifth peak around 220 K. Figure 4.8 only depicts doses less than 4 M/UC as the monolayer coverage likely is equivalent to the four surface Fe_{oct} atoms in the unit cell, probably acting as adsorption sites. The first peak at 130 K grows individually until 0.46 M/UC. It is joined almost immediately by the second peak at 110 K from 0.61-1.83 M/UC. The third peak at 95 K then emerges and increases up to 3.21 M/UC. A fourth peak at 80 K builds until 3.67 M/UC, just before the multilayer peaks develop. The peak at approximately 220 K grows consistently with the dose, whereas the other four peaks eventually saturate. Due to saturation at low fractional coverages, the peaks at 130 K and 220 K are most likely related to surface defects.

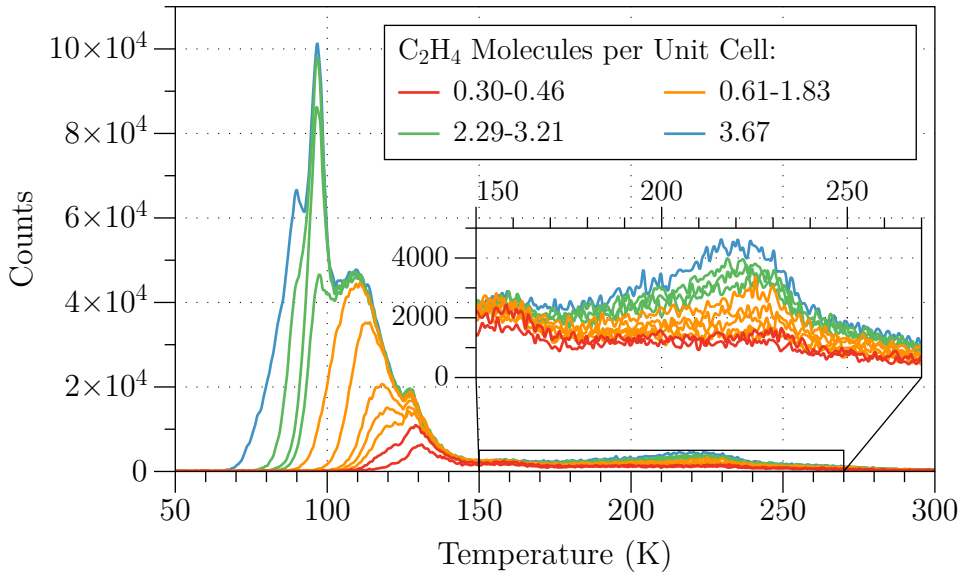

Figure 4.8: TPD spectra up to a coverage of one monolayer (4 C_2H_4 per unit cell) are displayed. The defect peak at 220 K is magnified. It grows with increasing coverages. The monolayer peaks are located at 80, 95, 110, and 130 K. They saturate at a certain coverage in contrast to the defect peak.

The TPD series was carried out in random order, so that possible changes in the surface do not incorrectly appear to correlate with increases in coverage. Furthermore, XPS data also support that standard preparation is not necessary between back-to-back C_2H_4 TPDs, at least when heated up to 680 K. In figure 4.9, the Fe2p XPS spectrum is depicted. The spectra shown were measured directly before and after a C_2H_4 TPD from 60 K to 680 K. The normalized spectra are visibly identical within a given range

allowing for noise. The same holds true for the O1s spectra before and after the C_2H_4 TPD seen in figure 4.10.

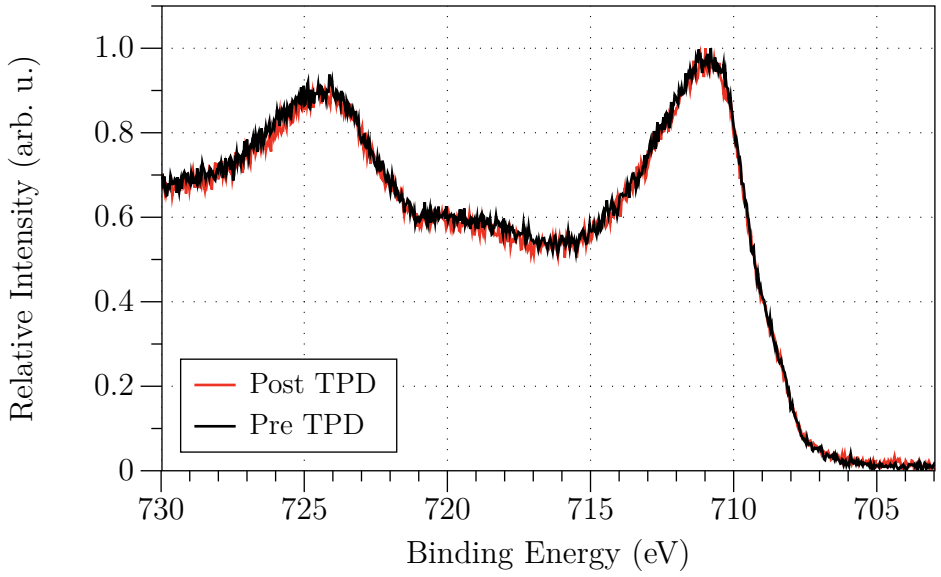

Figure 4.9: The Fe2p grazing-emission XPS spectrum is shown before and after a C_2H_4 TPD from 60 K to 680 K.

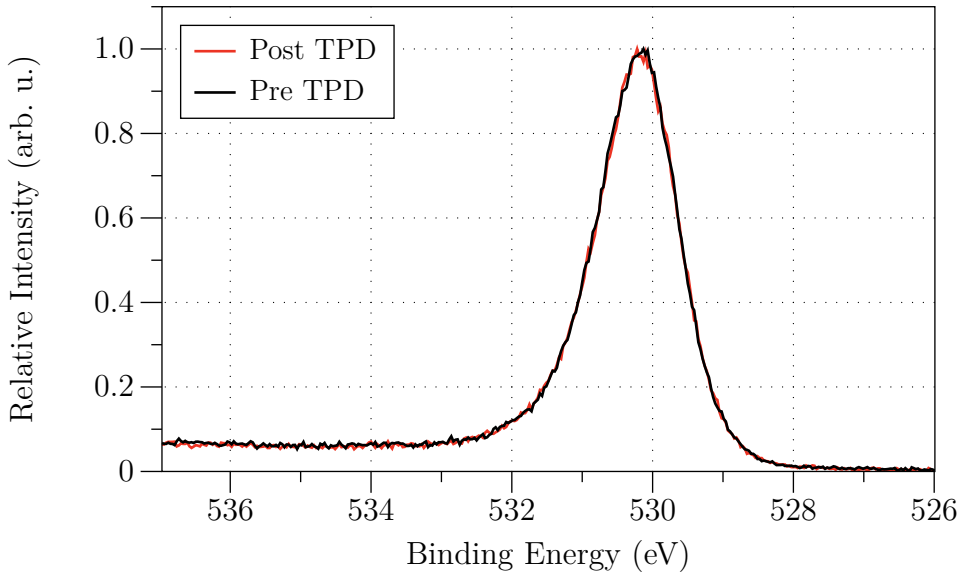

Figure 4.10: The O1s grazing-emission XPS peak is shown before and after a C_2H_4 TPD from 60 K to 680 K.

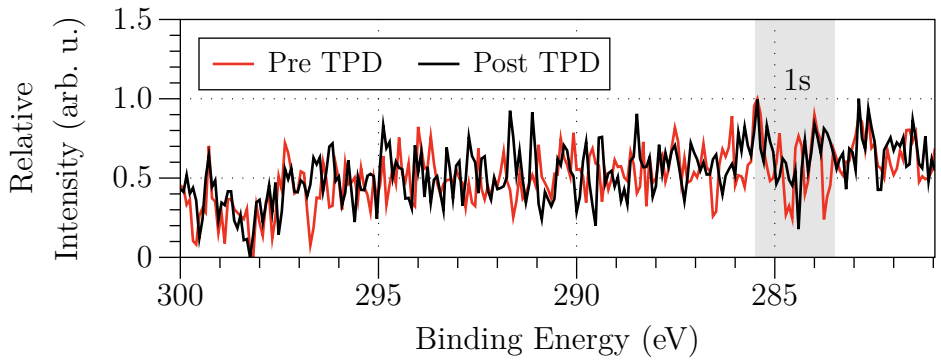

Figure 4.11: The C1s grazing-emission XPS spectrum is shown before and after a C_2H_4 TPD from 60 K to 680 K. The sample is free of carbon in both cases.

Carbon contamination can be disregarded on basis of the C1s spectra seen in figure 4.11. There is no peak-like feature that can be discerned from the background noise. It is worth noting that the data labeled "Pre TPD" in figures 4.9 to 4.11 could also be labeled "Post Standard Prep" as a standard preparation cycle was carried out directly before XPS. Additionally, TPD spectra of identical doses of C_2H_4 were taken within the TPD series that is represented in figures 4.6 to 4.8. They can be seen in figure 4.12. Again, the spectra show the same desorption behavior within a small margin of error.

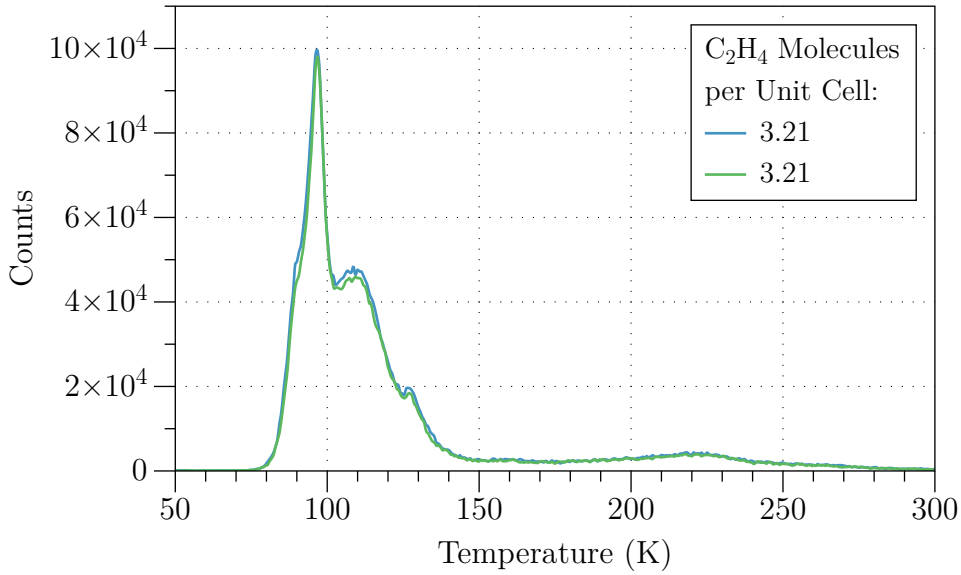

Figure 4.12: Two TPD spectra with a dose of 3.21 C_2H_4 per unit cell carried out toward the beginning and the end of the otherwise randomized series of back-to-back C_2H_4 TPD spectra. They are identical within a small margin of error.

4.1.4 The Effect of Heating Rate on C_2H_4 TPD Data

Figure 4.13 portrays three TPD spectra with multilayer coverages of 5.52 M/UC with heating rates of 0.1, 1.0, and 3.0 K/s. While there are some small differences, like the ratio of the intensities of the two multilayer peaks, the number of peaks is the same. The desorption temperatures also remain similarly spaced. Kinetics do not appear to take part in the monolayer desorption, while they likely do take part in multilayer desorption. This is important because this signifies the sample is not cracked, which could have been a cause for the double multilayer peak.

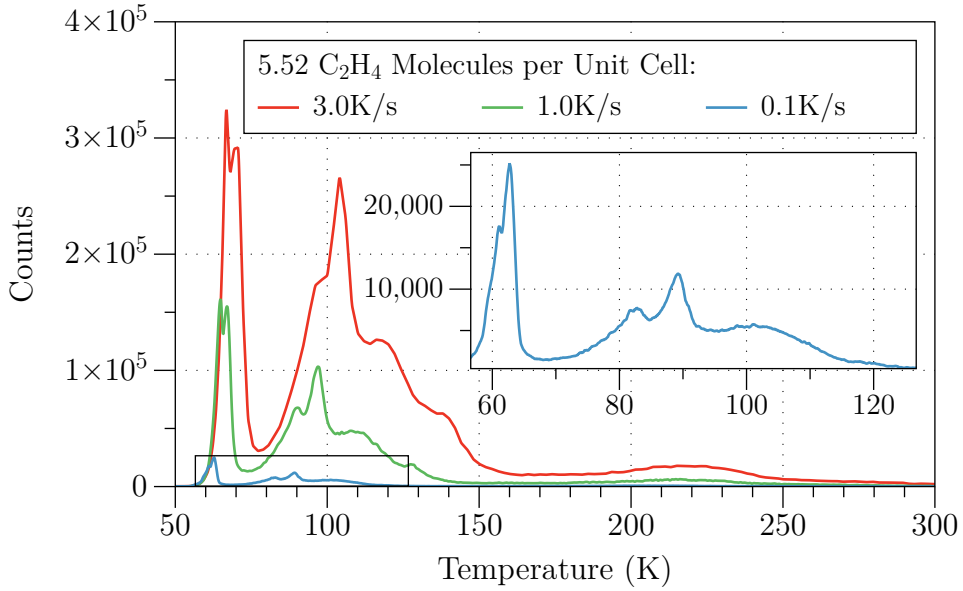

Figure 4.13: Three TPD spectra with multilayer coverages of C_2H_4 are depicted, with heating rates of 0.1, 1.0, and 3.0 K/s. The shape of the spectra barely changes with regard to heating rate. The biggest change is seen in multilayer peak ratios, indicating that kinetics only play a role for multilayer desorption.

4.1.5 XPS and UPS Data of C_2H_4 on Fe_3O_4(001)

To conclude investigation of C_2H_4 on the clean surface, XPS and UPS data were gathered while C_2H_4 was adsorbed on the surface. Figure 4.14 depicts XPS spectra of two of differing C_2H_4 coverages, the clean surface, and a post-anneal state. All spectra were taken at 60 K. The latter two spectra appear identical, suggesting that flashing the sample to 400 K is enough to desorb the ethylene. The spectra of 1.2 L and 10.0 L of C_2H_4 contain the expected C1s peak, but also a satellite peak approximately 8.3 eV above the primary peak. The satellite peak grows proportionally to the primary peak,

suggesting it is not the result of contamination. It also corresponds to the energy of a Rydberg excitation ($\pi \rightarrow 3p$) of the C_2H_4 molecule [37–42].

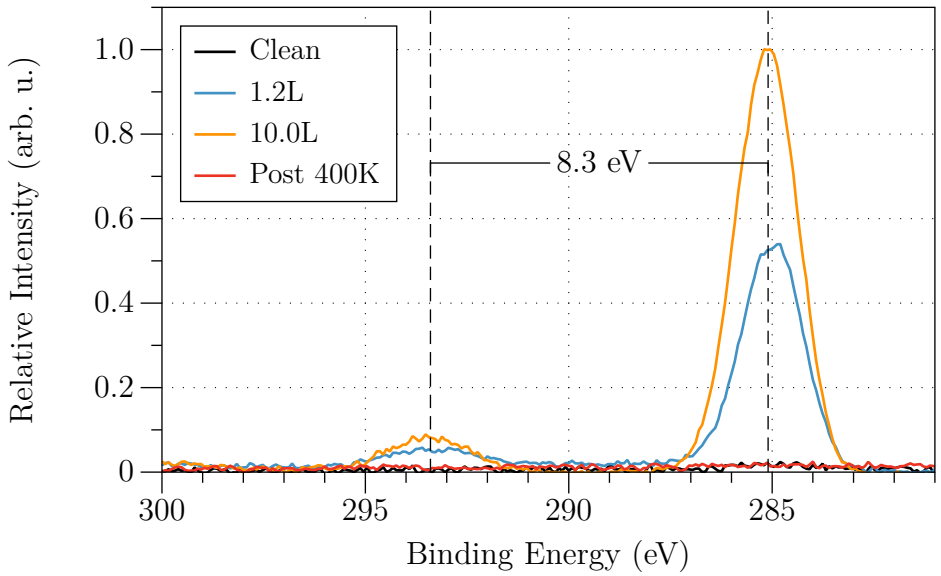

Figure 4.14: The C1s core levels were analyzed with grazing-emission XPS at 60 K after dosing C_2H_4. The satellite peak at 293.2eV is clearly visible and the 8.3 eV shift corresponds to a ($\pi \rightarrow 3p$) Rydberg excitation in the C_2H_4 molecule [37–42].

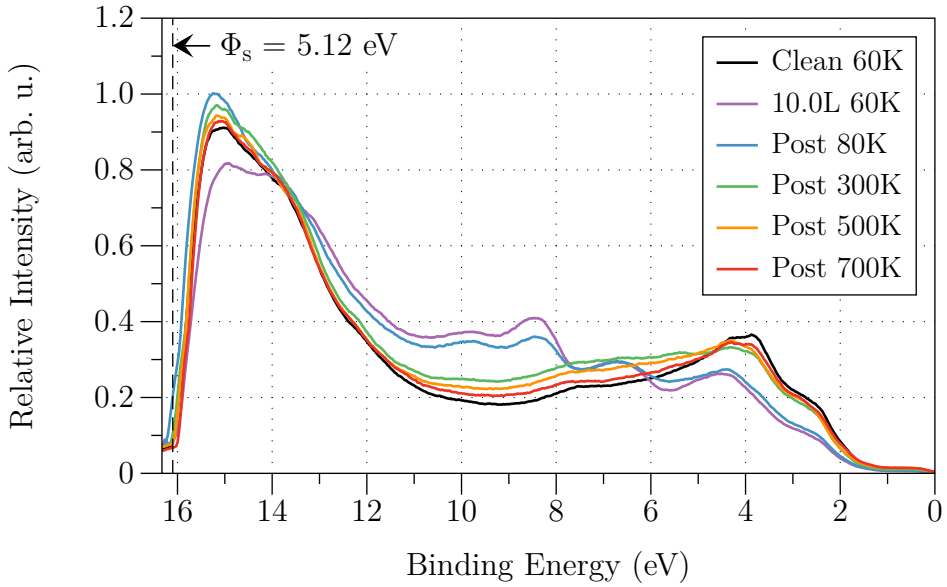

Figure 4.15: Grazing-emission UPS spectra, taken at 60 K, of the clean surface and various coverages of C_2H_4 are shown. After 10.0 L of C_2H_4 were dosed at 60 K, the sample was heated to temperatures of increasing magnitude to desorb some C_2H_4.

After an UPS spectrum of clean $Fe_3O_4(001)$ was taken, 10.0 L of C_2H_4 were dosed at 60 K. Subsequently the sample was heated to temperatures in order of increasing magnitude to desorb some C_2H_4. The sample was cooled down to 60 K before each UPS measurement. The results can be observed in figure 4.15. The work function of the $Fe_3O_4(001)$ surface was calculated on basis of the He-I line (21.2 eV). The resulting 5.12 eV are not identical to the values (5.3 eV,5.5 eV) measured by J. Hulva, however due to the ill-defined secondary electron cutoff the results are not in conflict [31]. Another reason for the difference is that the sample was not biased to decouple the work function of the analyzer. In contrast to the XPS data shown in figure 4.14, UPS results of the clean surface and a post-anneal state after a 400 K flash do not coincide. Only flashing to approximately 700 K recovers the original UPS spectrum. Note that all TPD spectra are measured up to 680 K.

4.1.6 C_2H_4 on Rhodium Adatoms on $Fe_3O_4(001)$

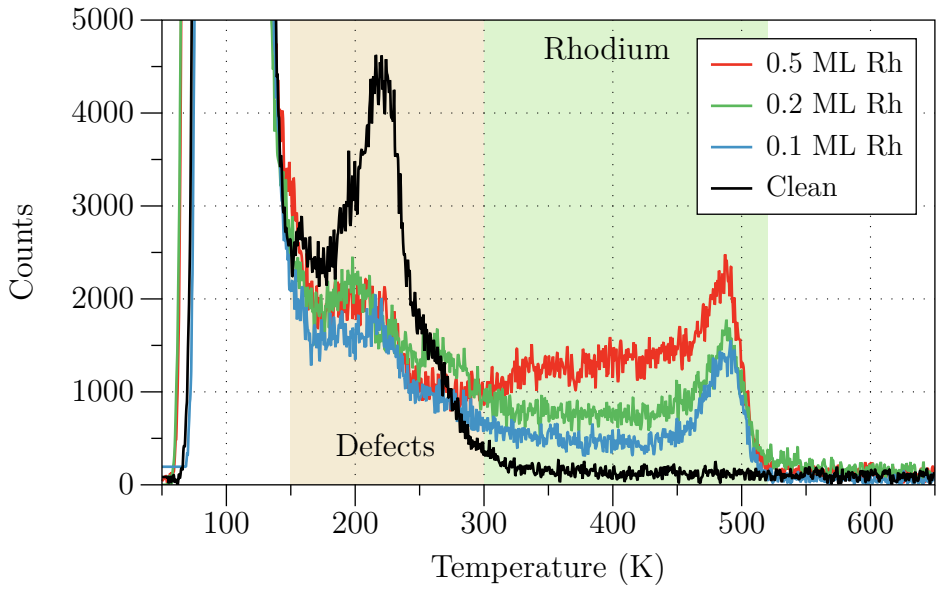

Figure 4.16: TPD spectra of monolayer coverages of C_2H_4 on $Fe_3O_4(001)$ with various coverages of rhodium are depicted. The high temperature peak around 480 K is elevated by a tail starting at 300 K and is attributed to C_2H_4 adsorbed on Rh.

After studying C_2H_4 on the clean $Fe_3O_4(001)$ surface, investigation was continued in the presence of various sub-monolayer coverages of rhodium. In this work, one monolayer is defined as one rhodium atom per $Fe_3O_4(001)$ unit cell. Preparing the rhodium coverage involved standard preparation followed by evaporation of rhodium

onto the sample at 300 K. The calibration was performed with a QCM in order to determine the time required for the desired coverage. Each measurement requires re-preparation due to the incorporation[3] of rhodium above 420 K [31]. Figure 4.16 shows four magnified C_2H_4 TPD spectra. For each spectrum, the sample was cooled to 60 K after preparation. The spectrum measured on the clean surface contains its highest temperature peak around 220 K which tapers off to 300 K. Beyond this temperature, only noise can be observed. In contrast, the spectra measured with 0.1, 0.2, and 0.5 ML of rhodium contain desorption peaks above this temperature. There is a distinct peak at approximately 480 K for all three rhodium coverages. Above 0.1 ML of rhodium, the peak develops a prominent tail down to 300 K, and the entire range between 300-480 K increases in intensity. Simultaneously, the peak in the region "Defects" shrinks in intensity as rhodium coverage increases. This region has been labeled "Defects", because it saturates at a fractional coverage of C_2H_4, far below 1 M/UC.

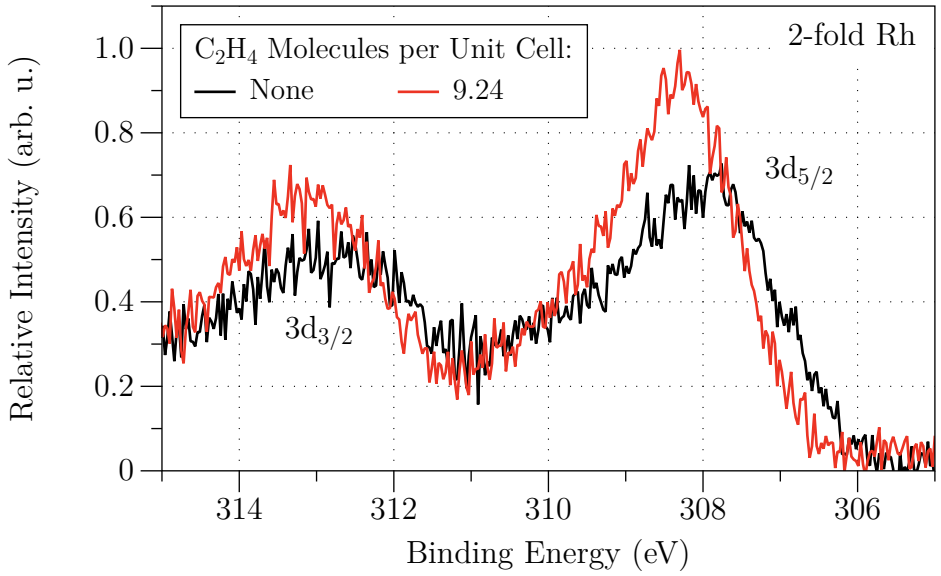

Figure 4.17: The core level shift of the Rh3d peaks with adsorbed C_2H_4 versus the reference spectrum can be observed in this graph. Both spectra were measured at 300 K under grazing-emission with 0.2 ML of rhodium on the surface.

Since the adsorption site cannot be determined from TPD spectra alone, XPS measurements were performed in order to gather information about the core-level shifts of the rhodium photoelectron lines. The results are displayed in figure 4.17. First 0.2 ML of rhodium were deposited and the reference spectrum was measured. Then 9.24 M/UC of C_2H_4 were dosed and XPS was measured again, showing a shift of approximately

[3]Rhodium adsorption and incorporation have been treated in the introduction. See figure 1.8.

0.6 eV. This suggests the C_2H_4 is adsorbed on the rhodium. A temperature of 300 K was maintained throughout the experiment. Notably, rhodium can also incorporate in the subsurface layers with a 5-fold coordination [30, 31]. Thus, another question is whether the C_2H_4 adsorbs to the 5-fold coordinated rhodium.

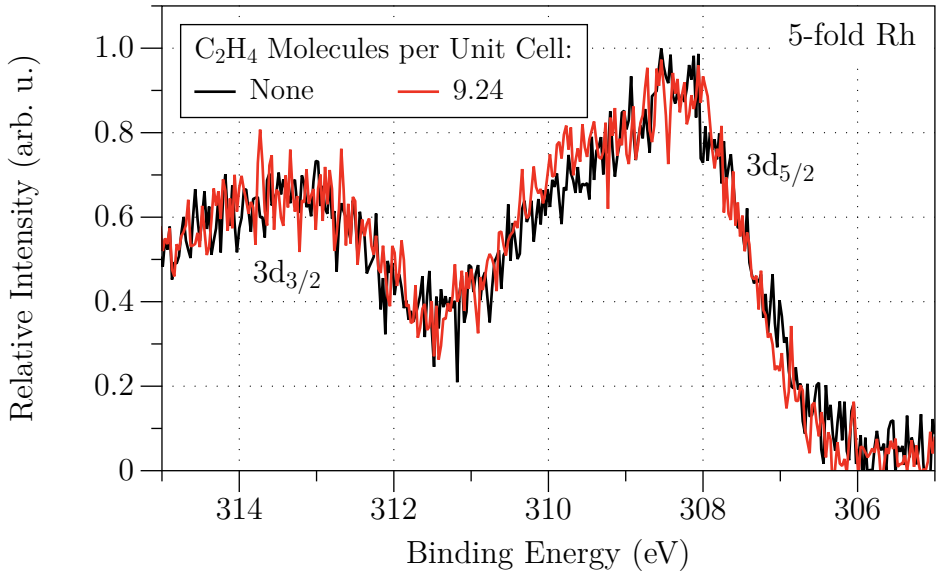

Figure 4.18: Grazing-emission XPS measurements of the Rh3d core levels suggest that adsorption of C_2H_4 on the 5-fold site is not possible. Heating to 420 K for five minutes after dosing 0.2 Ml of rhodium results in the baseline spectrum, which is unchanged after dosing 3.0 L of C_2H_4 at 300 K.

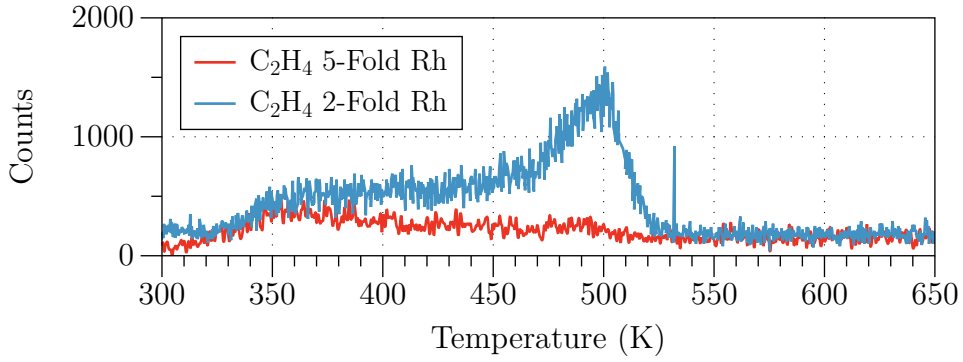

Figure 4.19: TPD spectra of attempted C_2H_4 adsorption on 2-fold and 5-fold rhodium sites at 300 K are shown. 0.2 Ml of rhodium have been deposited beforehand. The incorporation into the 5-fold site was achieved by annealing to 420 K for 5 minutes.

Formation of the 5-fold site was induced by annealing the sample to 420 K for five

minutes after depositing 0.2 ML of rhodium at 300 K. XPS analysis was carried out as for the 2-fold site, and the spectra are portrayed in figure 4.18. First, a baseline XPS spectrum (without C_2H_4) after annealing was measured. It shows a distinct increase in intensity between binding energies of 309 to 310 eV relative to the baseline spectrum in figure 4.17. This is consistent with the findings of J. Hulva and R. Bliem, and signifies the desired incorporation of rhodium has been achieved [30, 31]. Then 3.0 L of C_2H_4 were dosed onto the surface, and another XPS spectrum was measured. In contrast to the 2-fold site, there is no change in the Rh3d peak profile, suggesting that C_2H_4 cannot adsorb onto 5-fold coordinated rhodium. This is consistent with the TPD data displayed in figure 4.19.

4.2 Coadsorption of C_2H_4 and $C^{13}O$ on Fe_3O_4(001)

Coadsorbing CO with C_2H_4 on Fe_3O_4(001) in the presence of rhodium adatoms adds another layer of complexity. As before, TPD and XPS are employed for analysis. Isotopically labeled $C^{13}O$ (mass 29) was used to differentiate it from background CO (mass 28), as well as to avoid overlap with the main mass of C_2H_4 (also 28).

4.2.1 Coadsorption at Low Temperature (60K)

The initial scientific effort was dedicated to low-temperature coadsorption, both for consistency with previous data as well as the fact that temperature is a separate parameter to vary. First, reference TPD data of CO was gathered, as depicted in figure 4.20. Since the high-temperature features are of relevance, the TPD spectra are magnified to show the smaller features above 300 K. The figure contains a TPD spectrum of CO on the clean surface, exhibiting similar behavior above 300 K as the clean spectrum of C_2H_4 in figure 4.16. Specifically, there are no significant features. Equally, the spectrum of CO on 0.2 ML of rhodium also behaves like C_2H_4 on 0.2 ML of rhodium, with a peak emerging at higher temperature. The CO peak at 560 K is 20 K higher than expected according to J. Hulva, however the disparity is reconciled when considering the mounting position of the thermocouple (see the discussion for details) [31]. The third spectrum contained in the figure was taken in presence of both 0.2 ML of rhodium as well as C_2H_4. It is the result of adsorbing 3.0 L of CO first, and then dosing 3.0 L of C_2H_4. Significantly, the shape of the TPD spectrum is akin to that of only CO on 0.2 ML of rhodium. While the intensity is slightly lower, this could be due to multiple reasons, all of which will also be considered in detail in the discussion. The following results will also show that the order of adsorption matters.

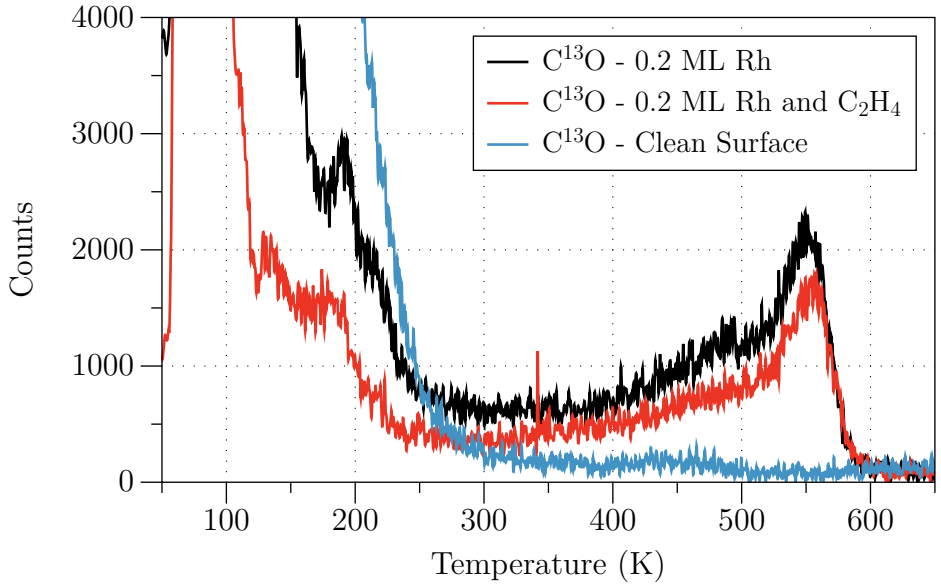

Figure 4.20: TPD spectra of monolayer CO coverages are magnified to show the peak correlated with rhodium adatoms. The clean surface shows no peak around 560 K, however, a peak develops in the presence of 0.2 ML of rhodium. Coadsorbing C_2H_4 after dosing CO in the presence of rhodium does not change the desorption temperature of the CO (560 K). Reasons for the lower intensity are laid out in the discussion.

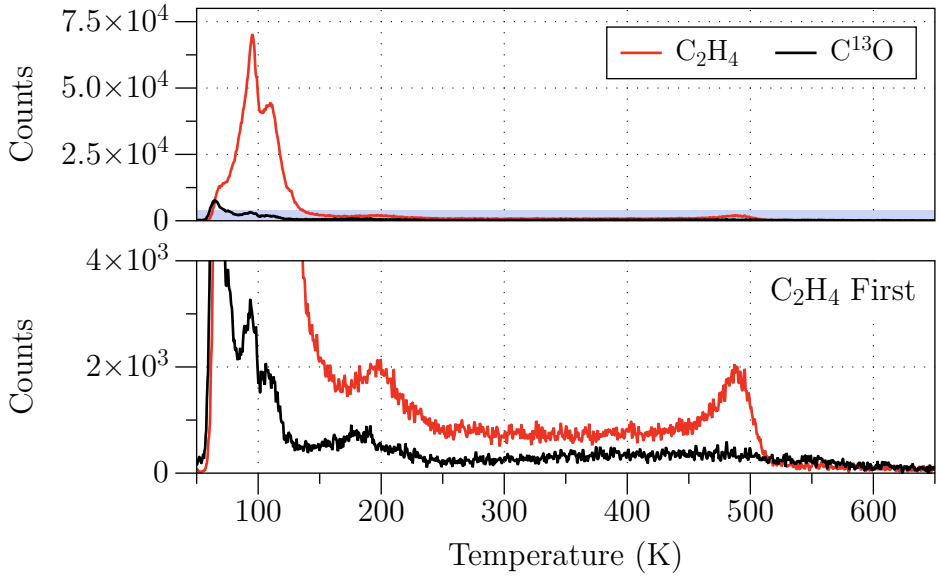

Figure 4.21: Coadsorption of C_2H_4 and CO on 0.2 ML rhodium is depicted. After cooling the sample to 60 K 1.2 L of C_2H_4 were adsorbed, followed by 1.0 L of labeled CO. The expected peak of C_2H_4 at 480 K can be clearly identified, while the high temperature peak of CO is missing. This suggests C_2H_4 blocks adsorption of CO. The bottom graph magnifies the blue area on top.

In the context of this thesis coadsorption does not imply concurrent dosing of both species, but rather that both species are dosed onto the sample within the same experiment. Naturally, either C_2H_4 or CO has to be dosed first, and data show that the order is significant. The result of adsorbing 1.2 L of C_2H_4 and then 1.0 L of CO at 60 K is shown in figure 4.21. The area highlighted in blue in the graph on top is magnified in the graph on the bottom. The peak and tail of the 480 K peak of C_2H_4 on rhodium is clearly visible, while the peak for CO on rhodium previously seen at 560 K in figure 4.20 does not appear. Nonetheless a long flat feature can be seen just above the background noise level between 300 K and 600 K. This could suggest some form of clustering. The opposite can be observed in figure 4.22. In this case 3.0 L of CO were dosed first, followed by 3.0 L of C_2H_4. While the C_2H_4 peak is approximately half as intense as in figure 4.16, the CO peak is not reduced in magnitude. This implies C_2H_4 blocks the adsorption of CO on rhodium, but not vice-versa.

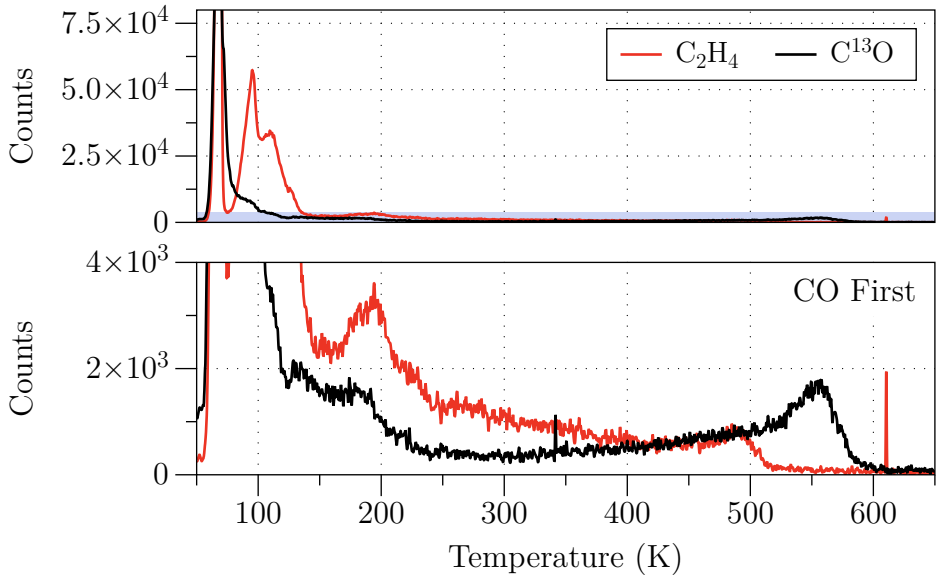

Figure 4.22: Coadsorption in presence of 0.2 ML rhodium is depicted. After cooling the sample to 60 K 3.0 L of labeled CO were adsorbed, followed by 3.0 L of C_2H_4 . Both masses have distinct high temperature peaks. This suggests CO has to be adsorbed first if coadsorption is desired. The spike above 600 K is an artifact. The bottom graph magnifies the blue area on top.

Additionally, the dosing process was always monitored with the mass spectrometer before each TPD experiment. While this data is mainly intended to confirm correct execution of the dosing process, it contains important information in the context of the coadsorption experiments. Figure 4.23 depicts the scenario in which CO was dosed

first, until saturation. The sharp increase in CO counts, toward the end of the area highlighted in blue, signifies that more CO is being reflected off the surface, typical of a saturated surface. When C_2H_4 is dosed, the CO signal strongly increases again, indicating displacement of CO by C_2H_4. Figure 4.24 shows the opposite scenario, however no increase in the signal of C_2H_4 is seen when dosing CO second. In both scenarios, the sample was at a temperature of 60 K with 0.2 ML of rhodium. Thus it is not immediately obvious, whether the CO monolayer is being displaced by C_2H_4, or if the CO molecules adsorbed to the rhodium adatoms are being displaced. However, the presence of the 560 K CO peak in all cases where C_2H_4 is dosed second, strongly supports displacement of CO molecules that are not on the rhodium adatoms, otherwise this peak should decrease in magnitude.

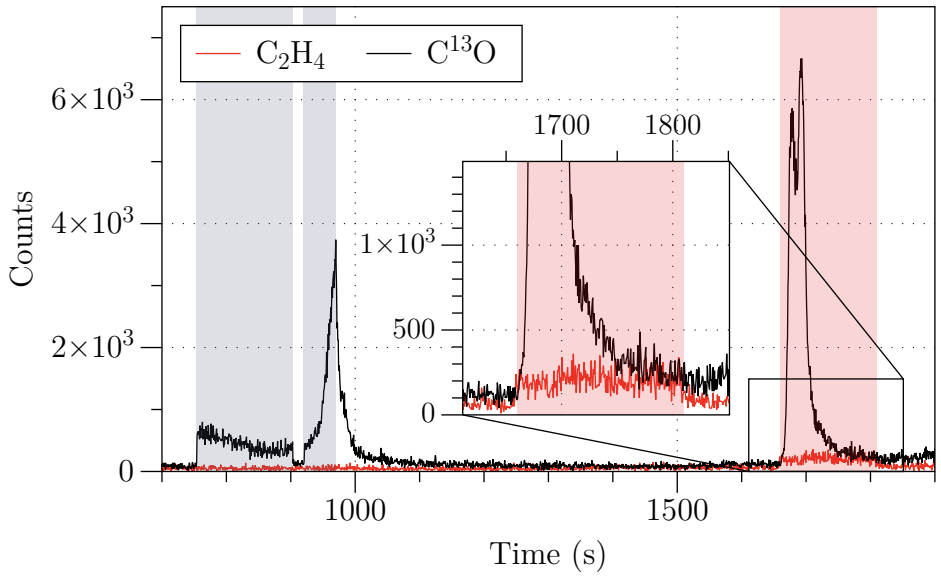

Figure 4.23: The dosing process is depicted. The highlighted regions mark the dosing window of their respective species. At 60 K CO was dosed until saturation, as the sharp increase in counts indicates CO being reflected off the surface. Then C_2H_4 was dosed after waiting until the reservoir was empty of CO, as judged by a pressure of 10^{-8} mbar. Only a small increase in counts of C_2H_4 is visible in the area highlighted in red. This is because the sticking coefficient is near unity at 60 K. Simultaneously CO desorbs from the sample as shown by the drastic increase in CO counts. This indicates displacement of CO by C_2H_4. Which site this occurs on is not clear on basis of this data alone.

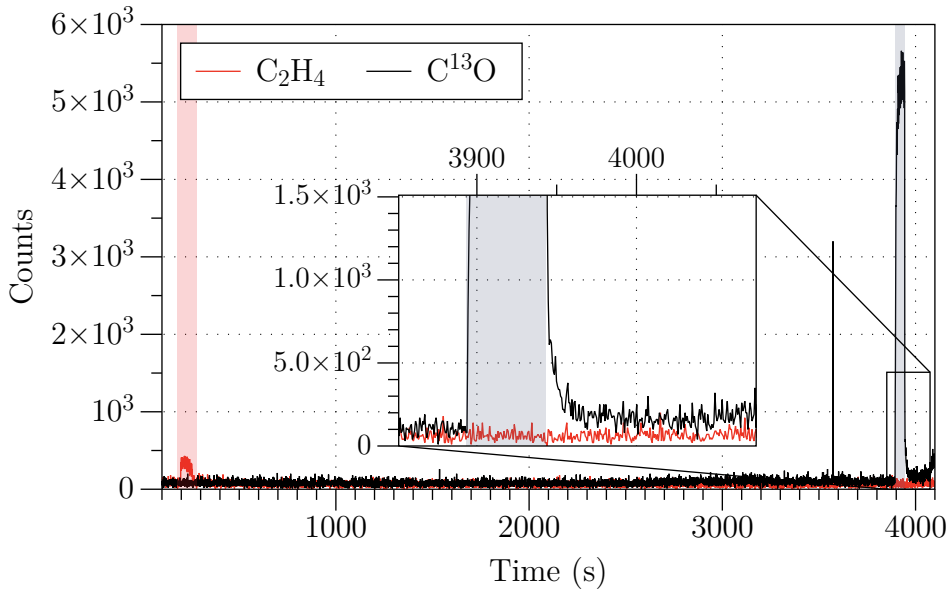

Figure 4.24: The dosing process is depicted. The highlighted regions mark the dosing window of their respective species. This time C_2H_4 was dosed first, then CO, both at 60 K. Since no increase in C_2H_4 counts is visible in the blue region, CO cannot be displacing C_2H_4.

4.2.2 Coadsorption at Room Temperature (300K)

Finally, coadsorption is attempted and analyzed at room temperature (300 K). Since there are no TPD peaks for CO or C_2H_4 above 300 K on the clean surface, all experiments are directly performed with 0.2 ML of rhodium on the surface. Both dosing orders are attempted, and the TPD spectra can be observed in figure 4.25. The upper graph shows the result of adsorbing CO first. Notably, the amount of CO adsorbed on the rhodium is the same as in the low-temperature case in figure 4.22, with the highest crest just below 2000 counts. A similar statement can be made about C_2H_4, however the background signal is much lower at 300 K since the monolayer contribution is missing, and thus absolute counts are not directly comparable. The lower graph shows C_2H_4 adsorbed first. This case is not as easily compared to the lower-temperature variant seen in figure 4.21, due to what appears to be a differing mass spectrometer sensitivity (see discussion for details). Nevertheless, the results are consistent with the data gathered from the low-temperature adsorption experiments, in the sense that C_2H_4 prohibits adsorption of CO, but not the opposite way.

Unfortunately, the small, uncontrollable variations in mass spectrometer sensitivity were taking place at random during the course of the experimental investigations. While they did not occur frequently, some spectra become difficult to compare, because of this.

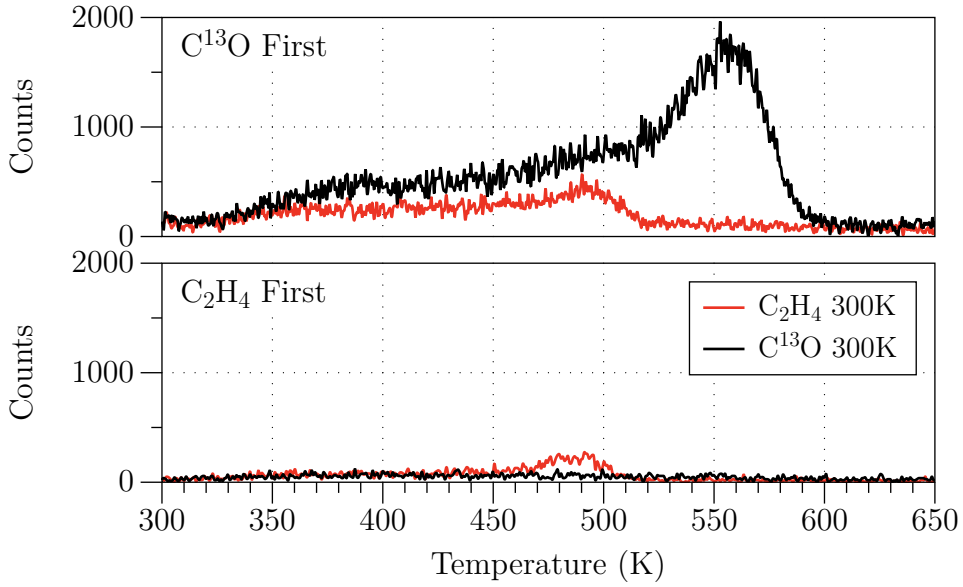

Figure 4.25: TPD spectra of coadsorption experiments at 300 K are shown. The upper graph shows CO first, the lower C_2H_4 first. Both are performed with 0.2 ML of rhodium.

An example can be seen in figure 4.26. In it, the C_2H_4 TPD spectra from figure 4.25 are juxtaposed, and the difference in noise and intensity levels is immediately visible. The fact that adsorbing C_2H_4 second leads to higher saturation is unlikely. This also hints some malfunction of the mass spectrometer. Both spectra were taken with emission currents of 500 mA, an electron-energy of 70 eV, and a secondary electron multiplier voltage of 2050 V. The fact that more masses were tracked in parallel to C_2H_4 in the case of C_2H_4 first as opposed to C_2H_4 second (the experiments were separated by two weeks time) is one of the few alternative explanations. The mass spectrometer sensitivity issues remain nevertheless.

Regardless, the important case is that in which the dosing order results in both species adsorbing to rhodium. The associated data set (top of figure 4.25) fortunately is comparable to previous data. The question whether C_2H_4 displaces CO in this case remains. In contrast to figure 4.23, which depicts the low-temperature behavior of this coadsorption order, figure 4.27 shows barely any displacement, if at all. In fact, the increase corresponds to roughly 200 counts upon dosing, which may also suggest minute contamination of the reservoir from the previously dosed $C^{13}O$. At the same time, the sticking coefficient of C_2H_4 also appears to be lower, as the C_2H_4 signal reflected off the surface into the mass spectrometer is higher than in figure 4.23. There must still be C_2H_4 adsorbing however, as the sticking coefficient measurement in figure 4.5 shows a purely "reflected" signal of C_2H_4 at 300 K off clean $Fe_3O_4(001)$ should produce a signal

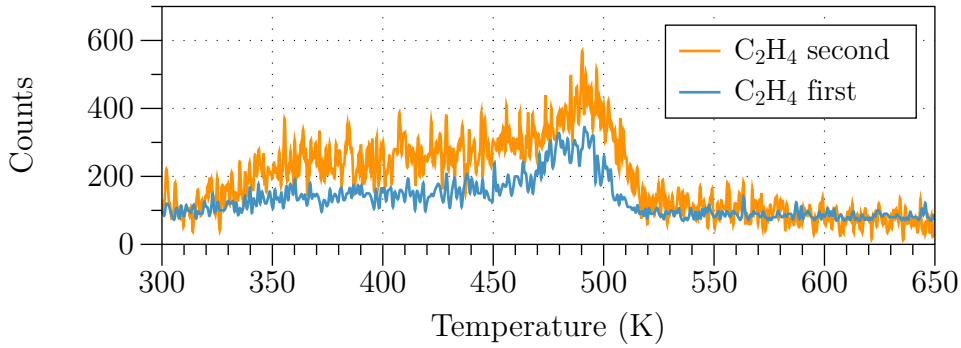

Figure 4.26: The C_2H_4 spectra from figure 4.25 are overlayed. Due to different sensitivity levels of the mass spectrometer the spectra cannot be compared in absolute intensity.

another 2.5x higher than the already increased signal. On basis of this approximation, the sticking coefficient of C_2H_4 in figure 4.27 is 28.6%. However, the sticking coefficient at this temperature should be near zero, as there is less than one rhodium atom per unit cell on average, and there are no monolayer adsorption sites available at 300 K. Therefore it is probable, that CO and C_2H_4 share a rhodium-based adsorption site on which they can also coadsorb. This scenario will be analyzed in detail in the discussion.

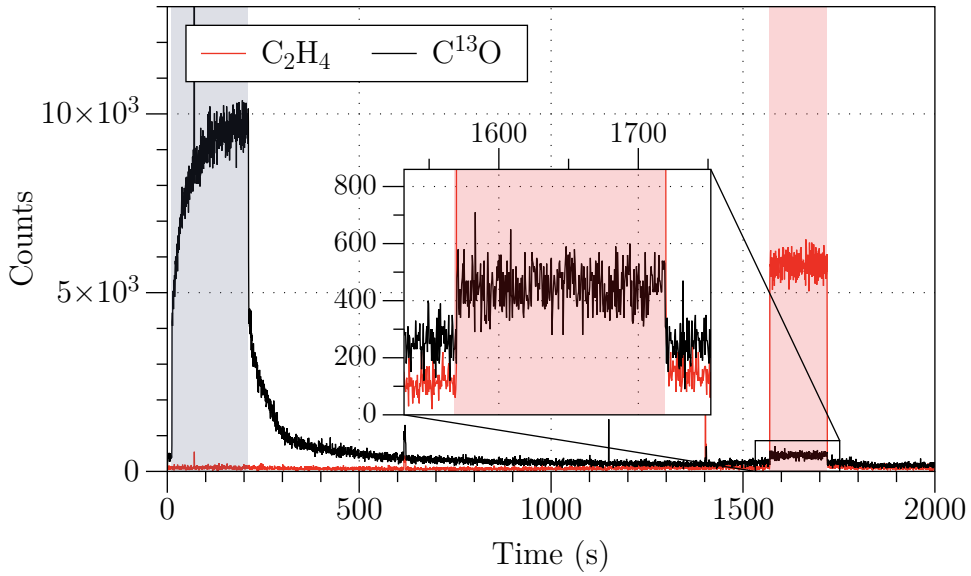

Figure 4.27: The dosing process at 300 K with 0.2 ML of rhodium is depicted. The highlighted regions demarcate the dosing window of their respective species. CO was dosed until saturation, followed by C_2H_4. The amount of C_2H_4 dosed (9.24 molecules per unit cell) is more than enough to saturate the high-temperature rhodium peak.

So far coadsorption experiments have only been performed on the 2-fold rhodium site, however it makes sense to attempt coadsorption on the 5-fold site at 300 K for completeness. Preparation involved annealing the sample at 420 K for five minutes after evaporating 0.2 ML of rhodium onto it as before. The outcome can be observed in figure 4.28. The graph shows the attempt at coadsorption by dosing CO first, followed by C_2H_4. Again the 480 K peak is missing. Only this order of coadsorption was attempted, as previous data already shows that C_2H_4 alone cannot adsorb to the 5-fold site. Evidently, it is not possible to adsorb C_2H_4 on the 5-fold coordinated rhodium site after dosing CO either.

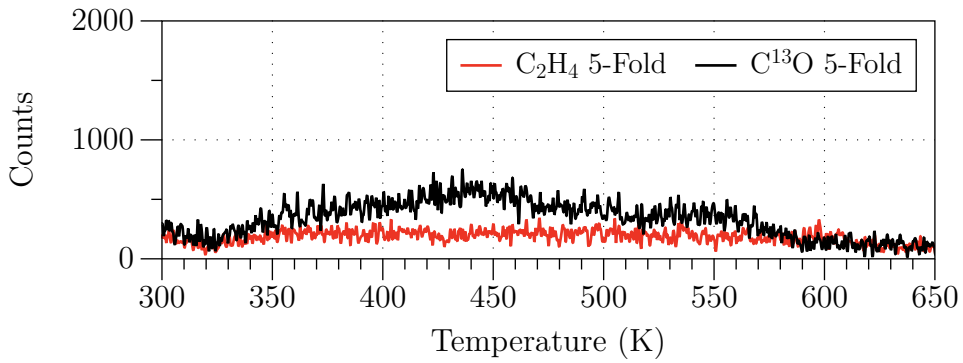

Figure 4.28: TPD spectra of attempted CO and C_2H_4 coadsorption on 5-fold Rh sites are shown. Unsurprisingly, the high temperature peaks of both species are missing.

5 Discussion

Adsorption of C_2H_4 on clean Fe_3O_4(001)

In order to understand the adsorption of C_2H_4 on Fe_3O_4(001) a series of TPD spectra of various coverages of C_2H_4 was measured first, followed by determination of the sticking coefficient. Coverages ranging from 0.10 L to 3.00 L of C_2H_4 were adsorbed at 60 K, and then desorbed with a heating rate of 1.0 K/s, up to 680 K. Combined with the calculation of the particle flow onto the sample, as shown in section 3.1, and correction of the doses by the sticking coefficient shown in section 4.1.2, this led to the TPD spectra depicted in figures 4.6-4.8. The doses in Langmuir have been converted to a more intelligible number of C_2H_4 molecules per Fe_3O_4(001) unit cell (0.32-9.24 M/UC). The TPD spectra were measured in random order, so that possible effects of multiple back-to-back TPD measurements do not appear to correlate with C_2H_4 coverage. XPS spectra in figures 4.9-4.11 also support that individual TPD measurements do not modify the surface. Further evidence of this is shown in figure 4.12, which overlays two TPD spectra of the same C_2H_4 coverage, only differing by noise, taken toward the beginning and the end of the series.

Figure 4.6 shows an overview of the TPD series. The largest peak at the lowest temperature is the multilayer peak, as determined by its continual growth above 4.13 M/UC. It exhibits an unusual feature, namely the parallel growth of two peaks between coverages of 4.13-7.38 M/UC, which merge into one peak at higher coverages. The reason for this is not entirely clear. In any way, kinetics play a significant role and if the TPD heating rate is slow enough, the lower temperature peak is minimized, meaning the molecules are restructured into the "regular" multilayer structure (see figure 4.13). The reason for this likely is that the Fe_3O_4(001) unit cell lattice parameter (8.397 Å) does not match any of the surfaces that could be created from the body-centered monoclinic unit cell of crystalline C_2H_4 (a = 4.63 Å, b = 6.62 Å, c = 4.07 Å, β = 94.5°) [43, 44]. Further support for this is provided by the fact that monolayer coverage is highly likely equivalent to 4 M/UC since it has to be a number of molecules between 4.13 and 3.67 according to TPD data, and the four Fe_{oct} iron cations on the unit cell surface likely act as adsorption sites. Merging of the dual multilayer peak occurs at the equivalent of two monolayers (7.84 M/UC) which would be consistent with the second layer of C_2H_4 being a transition layer between the monolayer on the Fe_3O_4(001) surface and the third

layer which should already resemble crystalline C_2H_4. While DFT simulations could provide further information on this subject, the coverages of a monolayer or less are more relevant for the following coadsorption studies.

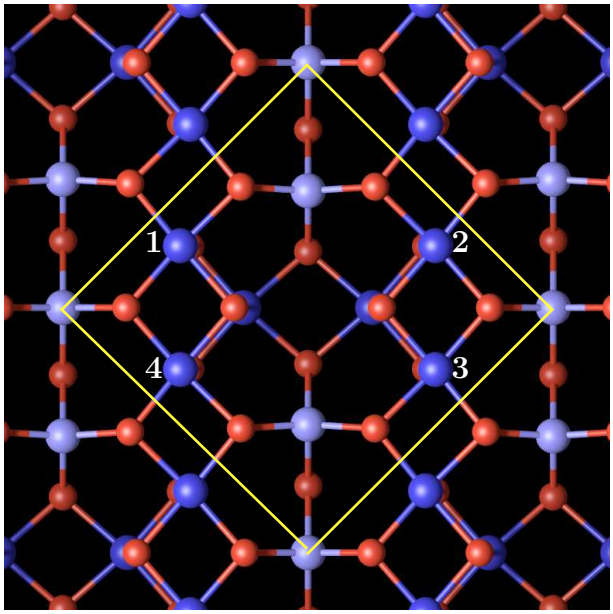

Figure 5.1: The unit cell of $Fe_3O_4(001)$ with labeled atoms in the iron rows. Based on the TPD desorption peaks there are approximately 4 C_2H_4 per unit cell, two of which have equal desorption energies since the monolayer peak at 130 K saturates at 2 molecules per unit cell. This means the first two C_2H_4 molecules likely adsorb on opposite iron rows. The left iron "row" consists of atom 1 and 4, while the right consists of 2 and 3. The 3rd and 4th C_2H_4 molecules have lower desorption energies, indicating that there is some change in the adsorption geometry (rotation/translation) as opposed to the first two molecules. They probably adsorb on the remaining two sites.

The C_2H_4 monolayer can be observed in detail in figures 4.7 and 4.8. Figure 4.7 displays the highest desorption peak at 220 K. Figure 4.8 encompasses only the spectra with coverages up to a monolayer, magnifying five desorption peaks in the range of 80-220 K. The peaks at 130 and 220 K are saturated at fractional coverages far below 1 M/UC, indicating that they likely originate from surface defects such as antiphase domain boundaries in the surface reconstruction and/or step edges. The three remaining peaks at 80, 95, and 110 K would therefore be attributed to the adsorption of C_2H_4 on the clean $Fe_3O_4(001)$ unit cell. As before, TPD data is not enough to determine adsorption location or geometry, however a few possible geometries can be hypothesized on basis of the desorption peaks and the fact that 4 C_2H_4 molecules have to fit into the $Fe_3O_4(001)$ unit cell. There are four octahedral iron atoms on the surface in the unit cell, labeled 1-4 in figure 5.1. It is probable, that the double C-C bond positions

itself over one of these iron atoms. When populating the unit cell with C_2H_4 the lower coverage peak at 110 K is saturated first at 1.83 M/UC, signifying there are two adsorption sites in the unit cell with equivalent desorption energies. While this does not provide information about the orientation of the molecule, it would make sense if the first two C_2H_4 molecules adsorb on opposite iron rows. This would mean one C_2H_4 is on site 1 or 4 in figure 5.1 while the other is on site 2 or 3. Diagonally opposite combinations would be (1,3) or (2,4) putting the most distance between individual C_2H_4 molecules. Note this is purely speculative, and the system should be relaxed by DFT and imaged with scanning-tunneling microscopy or atomic-force microscopy for further information.

The next peak is saturated slightly below 3.21 M/UC at a lower desorption temperature of 95 K. In other words, the third C_2H_4 molecule is easier to desorb, for example because the third adsorption site forces the other two molecules to shift or reorient slightly. Returning to figure 5.1, if sites 1 and 3 are already blocked by the first two C_2H_4 molecules, the third C_2H_4 molecule could adsorb at 2 or 4. Continuing this hypothesis for the case of adsorption in site 2, the iron atom above site 2 would lie in the next unit cell at the top left and be equivalent to site 4. Since it was assumed the first two molecules adsorb to site 1 and 3, this would be the last site free of C_2H_4 (for the purpose of example). This would be in agreement with the third peak saturating at 4 C_2H_4 molecules at yet a lower temperature of 80 K, since the last C_2H_4 would have to reorient and shift three neighboring, already adsorbed molecules. The example can be extended to all symmetry equivalent sites within the plane symmetry group CMM of the $Fe_3O_4(001)$ surface.

Estimating the 2D C_2H_4 density from the previously mentioned unit cell gives an approximate number to compare the monolayer coverage to. There are two approaches to this estimation. One is to calculate the 3D density of the unit cell (with two C_2H_4 per unit cell volume), take the cube root for an effective 1D density, and square that for an effective 2D density. This results in 4.5 C_2H_4 per $Fe_3O_4(001)$ unit cell surface area. This approach is an overestimation, because it basically flattens the 3D unit cell onto a 2D surface, ignoring the orientation of the C_2H_4 molecules. Another is to use the side of the unit cell as a surface with one C_2H_4 per surface. For the surface with side lengths A and B this results in 2.3 C_2H_4 per $Fe_3O_4(001)$ unit cell surface area. The second approach is an underestimation as it restricts all C_2H_4 molecules to the same orientation (as in the crystalline C_2H_4 unit cell) and does not consider possible reorientation of individual C_2H_4 molecules on the $Fe_3O_4(001)$ surface. Since a monolayer coverage of 4 M/UC lies in between 2.3 and 4.5 M/UCthese estimates are in agreement with TPD data. Especially since neither estimate considers that the minimal nearest-neighbor distance in crystalline C_2H_4 is 4.07 Å, but the nearest-neighbor surface iron

atoms at a distance of 3 Å, likely requiring reorientation and/or shifting of the already adsorbed C_2H_4 molecules upon adsorption of the third and fourth C_2H_4 molecules.

After measuring the discussed TPD series, TPD spectra of C_2H_4 with different heating rates were taken, to examine if kinetics play a role in the desorption process. A dose of 5.52 M/UC was adsorbed at 60 K for each spectrum to provide a multilayer coverage that displays the dual multilayer peaks. The spectra with heating rates of 0.1, 1.0, and 3.0 K/s can be observed in figure 4.13. On one hand, the monolayer component of the spectrum maintains its shape and the relative ratio of desorption peaks as well as temperatures, indicating kinetics do not play a role. On the other hand, the ratio of the dual multilayer peaks shifts with heating rate, signifying that kinetics do matter during multilayer desorption.

In addition, XPS and UPS data was taken of different coverages of C_2H_4 adsorbed at 60 K. The C1s region was measured with XPS at both a monolayer coverage (1.2 L or 3.67 M/UC) and a multilayer coverage (10.0 L or 31.1 M/UC) of C_2H_4 as seen in figure 4.14. The figure also contains spectra of a clean surface after standard preparation, and of a sample flashed to 400 K after adsorption of C_2H_4. Within the sensitivity of the XPS instrumentation, a flash to 400 K appears to clean the sample of C_2H_4. A shake-up feature (satellite peak) can be seen at a binding energy 8.3 eV higher than the main peak. It can be attributed to a Rydberg excitation of the C_2H_4 molecule [37–42]. UPS spectra of the surface were taken in a similar fashion, as displayed in figure 4.15. The clean surface was measured at 60 K, followed by dosing of 10.0 L (31.1 M/UC) and another UPS measurement at 60 K. The spectrum with 10.0 L of C_2H_4 adsorbed shows three new peaks between a binding energy of 6-11 eV as opposed to the clean surface spectrum. This should correspond to peaks in the density of states (DOS) of C_2H_4 as the 21.2 eV ultraviolet photons from the He-I source are effectively probing the top 21.2 eV (including the work function) of the DOS. Of course, this is the DOS of the $Fe_3O_4(001)$ surface with C_2H_4 on it, so a simulation of the entire quantum mechanical system, far beyond the scope of this thesis, would be required to provide insight about which orbitals correspond to which peak. Afterwards the surface was flashed to 80, 300, 500, and 700 K, with another UPS measurement at 60 K in between each flash. The spectrum at 80 K should only include contributions from a monolayer coverage of C_2H_4, at least in context of the previously discussed TPD spectra. The data also shows slightly less developed peaks in the range of 6-11 eV compared to the previous spectrum. After flashes to 300, 500, and 700 K the peaks in this range disappear entirely, and the UPS spectrum gradually returns to that of the clean surface. In contrast to XPS data, this suggests a flash to 400 K is not sufficient to clean the surface and return it to its previous state. In fact, flashing to 700 K is necessary to remove the C_2H_4 features from the UPS spectra. This is consistent with TPD data so far, however. The TPD

spectra were taken in a range of 60-680 K, and subsequent TPD spectra did not appear influenced by previous spectra, likely due to the final temperature. Note that the UPS data can also be used for measurement of the work function of the surface, as explained in section 2.3. The work function was measured to be 5.1 eV, which does not agree with the 5.3-5.5 eV measured by J. Hulva in his thesis [31]. In hindsight, a small but significant error appears to have been made during the measurement. The sample was not biased for the UPS spectra taken in figure 4.15, meaning that the secondary electron cutoff is not representative of $E_{max} - E_{min}$, reconciling the disparity.

Adsorption of C_2H_4 on Rhodium Adatoms on Fe_3O_4(001)

Another layer of complexity was added to the adsorption process by involving isolated rhodium adatoms dosed onto the Fe_3O_4(001) surface. To shortly repeat the information presented on rhodium adatoms in the introduction: there are two sites on the Fe_3O_4(001) surface in which rhodium adatoms are stable. The 2-fold coordinated site is in the center of the unit cell, into which rhodium adatoms adsorb after dosing at low coverages. The 5-fold coordinated site is in the position of an octrahedral iron atom, which is replaced by the rhodium adatom upon annealing to 420 K. Both sites are visualized in figure 1.8. Annealing to higher temperatures does permit diffusion of rhodium into the bulk structure, however this is mainly relevant for sample (re-)preparation.

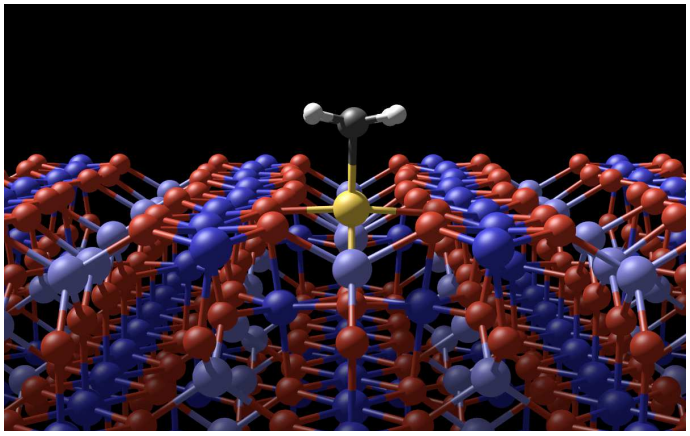

Figure 5.2: A render of C_2H_4 adsorbed on a 2-fold coordinated rhodium adatom as relaxed by DFT (optB88-DF, U_{eff} = 3.61 eV). The preliminary DFT calculations were performed by M. Meier.

First, TPD spectra of C_2H_4 dosed onto various coverage of rhodium were measured. Figure 4.16 contains spectra with 0.1, 0.2, and 0.5 ML of rhodium on the surface, as well as a clean surface spectrum for reference. Clearly, a peak develops at approximately 480 K, with a tail down to 300 K that grows with rhodium coverage. In parallel, the peak

at 220 K previously associated with defects decreases. This would make sense if rhodium adatoms preferentially saturate these defect sites, prohibiting C_2H_4 from desorbing off the defect sites. The tail above 300 K is more interesting because this means there have to be multiple desorption energies connected to C_2H_4 desorbing off rhodium adatoms, even if the primary peak is at 480 K. There are two major interpretations for this tail. One is that there are many different sites, possibly due to clustering of C_2H_4 around the rhodium adatoms. The second is that diffusion to a desorption site is somehow involved, meaning that differing amounts of energy have to be invested into desorbing C_2H_4 depending on how far away it is on the surface from a desorption site. Since TPD data does not suffice to support one scenario with certainty, imaging of the surface with STM and AFM as well as DFT calculations will be necessary in the future. Preliminary DFT calculations shows there is a stable adsorption site for C_2H_4 on the 2-fold site, as rendered in figure 5.2. XPS data shown in figure 4.17 supports the adsorption of C_2H_4 on the 2-fold site, as there is a clear shift in the Rh3d core level peak after dosing 9.24 M/UC. From this data however, it is not clear, whether this adsorption induces mobility of rhodium or not. The XPS spectra were measured with 0.2 ML of rhodium on the surface.

On the contrary, TPD and XPS data do not support adsorption of C_2H_4 on the 5-fold site. Annealing the sample at 420 K for 5 minutes after dosing 0.2 ML incorporates the rhodium from the 2-fold site into the 5-fold site. The XPS spectrum of the 5-fold coordinated rhodium without C_2H_4 is clearly shifted to higher binding energies in figure 4.18 versus the 2-fold baseline spectrum in figure 4.17. After dosing 9.24 M/UC of C_2H_4 onto the 5-fold coordinated rhodium, and measuring the Rh3d region again, there is no distinct difference in the new spectrum to the baseline spectrum. This hints at the inability of C_2H_4 to adsorb on the 5-fold site. The TPD spectra shown in figure 4.19 also provide evidence, that C_2H_4 can only adsorb to the 2-fold site, but not the 5-fold site. Careful observation of the figure shows that the desorption peak of C_2H_4 on 2-fold coordinated rhodium seems to be shifted up by 20 K relative to the 480 K peak in figure 4.16. This is likely due to the sample-sampleplate contact pressure decreasing over time, also decreasing thermal conductivity in parallel. In general, the thermal gradient between the thermocouple and the sample surface is a systematic error of the experimental setup, that can become worse over time. It is also the reason for the gold foil between the sample and the sampleplate, as this mitigates the issue. Another problem is the spotwelding of the thermocouple wires to the sample plate. Depending on the position of the thermocouple and the quality of the welding, the thermal gradient between the thermocouple and the sample plate can also change.

Coadsorption of C_2H_4 and CO on Rhodium Adatoms on Fe_3O_4(001)

Finally, coadsorption of C_2H_4 and CO on rhodium adatoms was investigated. Information about the surface chemistry of CO on rhodium adatoms on Fe_3O_4(001) similar to what has been gathered about C_2H_4 in this thesis so far, can be found in J. Hulva's dissertation [31]. TPD spectra of CO on clean Fe_3O_4(001) as well as with 0.2 ML were measured to provide reference data nonetheless. They are displayed in figure 4.20. The third TPD spectrum displayed in this figure is of CO adsorbed after dosing 0.2 ML of rhodium with coadsorption of a monolayer coverage of C_2H_4 at the end. Subsequent figures will show the order of adsorption and the rhodium site coordination matters, however a few more features of these CO spectra should be noted.

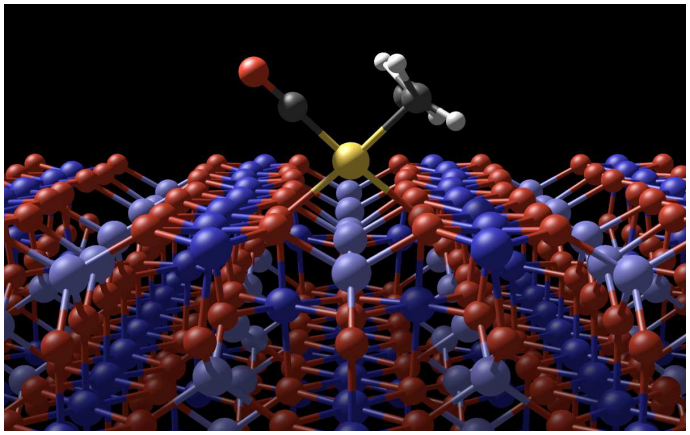

Figure 5.3: A render of C_2H_4 and CO coadsorbed on a 2-fold coordinated rhodium, as deemed the most stable by DFT (optB88-DF, U_{eff} = 3.61 eV). The preliminary DFT calculations were performed by M. Meier.

First, the CO peak at 560 K correlated with rhodium coverage, is 20 K higher than the peaks displayed in J. Hulva's data. As before, this likely has to do with the thermal gradient between the sample surface and the thermocouple, with the surface temperature lagging behind the thermocouple temperature. This means the thermocouple measures a higher temperature, but the sample surface is actually at a lower temperature, which is the temperature relevant for desorption. This error could likely be measured with a sufficiently precise pyrometer at higher temperatures. In any case, the temperature of the rhodium correlated desorption peak is located at the same temperature for both adsorption and coadsorption of CO in figure 4.20. The shape of the spectra is also nearly identical, speaking for the same adsorption site of CO on rhodium in both cases. The most obvious difference lies in the intensity, which is lower in the case of coadsorption. There are a few possible reasons for this. The first is that the amount of rhodium is not the same in both cases, as the difference would be approximately equal to 10-20%

difference in rhodium coverage. A QCM was used to calibrate the dose amount, and XPS was used to check relative amounts of rhodium, however this is within the uncertainty of the instrumentation at such sub-monolayer coverages. The second is that the mass spectrometer sensitivity changed over the course of the experiment even though the same parameters were used for measurement. Small changes in sensitivity of the mass spectrometer have been observed both within the course of this thesis as well as by other colleagues, unfortunately without an obvious pattern. Jumping ahead to figure 4.26, such a sensitivity difference can be observed. A third possibility for the intensity change is small differences in the surface due to sample preparation, again within the uncertainty of XPS spectra used to judge the state of the surface. The last reason could be that C_2H_4 displaces CO on rhodium and/or simply cannot coadsorb. This is unlikely due to the likelihood of the alternatives, as well as the fact that preliminary DFT calculations also show a stable coadsorption geometry for CO and C_2H_4 on the 2-fold site. This geometry is depicted in figure 5.3.

Coadsorption of C_2H_4 and CO onto the same rhodium adatom is also likely because TPD data show that the adsorption order matters. Figure 4.21 illustrates that adsorbing C_2H_4 at 60 K on 0.2 ML of rhodium before dosing CO prevents development of the 560 K peak for CO. Figure 4.22 depicts the opposite adsorption order, however in this case both the 480 K peak of C_2H_4 and 560 K peak of CO are visible. If C_2H_4 can block adsorption of CO on rhodium, then CO and C_2H_4 must share the same adsorption site on 2-fold coordinated rhodium adatoms. Considering the reduction of intensity of the high-temperature peaks, it would still be possible, that the two species adsorb on separate rhodium adatoms. Additional data does not support this interpretation, however. Figure 4.23 shows that displacement of CO is possible at 60 K, while figure 4.27 depicts this is not possible at 300 K providing evidence that displacement is only possible on adsorption sites associated with desorption temperatures below 300 K, namely the sites discussed in context of monolayer C_2H_4 coverage on clean $Fe_3O_4(001)$. Lastly, because C_2H_4 blocks CO adsorption when it is dosed first, the desorption peak intensity of C_2H_4 in the bottom case (C_2H_4 first) of figure 4.25 would have to be significantly higher than in the upper graph (CO first) as all the rhodium sites are available for adsorption. This does not appear to be the case, even with the sensitivity issues of the mass spectrometer. Admittedly, further techniques such as STM and AFM are required for a certain evidence of coadsorbed C_2H_4 and CO on rhodium. The final figure 4.28 depicts TPD data of attempted coadsorption of C_2H_4 and CO on 5-fold coordinated rhodium. C_2H_4 was adsorbed after CO since it is already clear that C_2H_4 cannot adsorb on a 5-fold site on its own. As expected, the 5-fold site does not permit coadsorption, because it is already coordinatively saturated in an octahedral site. This underlines the importance of the active site geometry in single-atom catalysis.

6 Summary and Outlook

On basis of the data gathered in the course of this thesis, extended studies of hydroformylation on single-atom catalysts in UHV seem feasible. A critical first step towards hydroformylation in UHV was demonstrated: the coadsorption of C_2H_4 with CO on isolated rhodium atoms on the $Fe_3O_4(001)$ surface. In order to arrive at this conclusion, investigation of C_2H_4 on the clean $Fe_3O_4(001)$ surface, as well as on isolated rhodium adatoms, was performed first. Subsequently coadsorption of C_2H_4 with CO was attempted. Data was gathered via TPD, XPS and UPS, with a standardized sample preparation procedure based on sputtering, annealing, and reoxidation in UHV.

TPD data shows a monolayer coverage of C_2H_4 on $Fe_3O_4(001)$ is equivalent to 4 M/UC, with desorption peaks at 80, 95 and 110 K. The first two sites have the same desorption temperature while the third and fourth C_2H_4 sites have lower desorption temperatures. The peaks at 130 K and 220 K saturate at coverages far below 1 M/UC, so they are attributed to surface defects, grain boundaries being an example of these. Further TPD and XPS measurements indicate that C_2H_4 can adsorb to isolated 2-fold coordinated rhodium adatoms, while it cannot adsorb to the 5-fold coordinated rhodium site. Data show this both for adsorption at 60 K and 300 K. In the presence of rhodium adatoms a desorption peak at 480 K develops in the TPD spectra. Preliminary DFT data predict a stable adsorption geometry of C_2H_4 on the 2-fold site, consistent with this data.

TPD and XPS data of coadsorbed C_2H_4 and CO on rhodium adatoms on $Fe_3O_4(001)$ were also gathered. While the order of adsorption clearly matters, as C_2H_4 blocks CO from adsorbing to the clean surface as well as rhodium adatoms if dosed before CO, it is not immediately obvious whether coadsorption on the same rhodium adatom is possible in the opposite adsorption order. Nevertheless data does show both species can be adsorbed to the surface, with preliminary DFT calculations also predicting a stable geometry for C_2H_4 and CO adsorbed to a 2-fold coordinated rhodium adatom. If coadsorption on the same rhodium adatom were not possible, only one species should show a high-temperature peak correlated with adsorption to rhodium in TPD spectra, or there are additional nontrivial adsorption sites not considered in this thesis. Within the data shown in this work there is sufficient evidence to conclude that coadsorption of C_2H_4 and CO on the same 2-fold coordinated rhodium adatom is likely, but additional

investigation by STM and AFM is necessary to acquire more conclusive evidence in favor (or in opposition) of this phenomenon.

Hydroformylation also requires atomic hydrogen on the surface, which was not investigated in the course of this thesis, but Dohnálek et. al show hydrogen splitting and spillover is possible on palladium adatoms on $Fe_3O_4(001)$ [45]. Combining palladium adatoms for hydrogen splitting with rhodium adatoms as active sites for hydroformylation would provide an interesting research opportunity on model single-atom catalysts in UHV. In summary, the research performed in course of the thesis is an important first step towards hydroformylation studies in UHV.

Bibliography

[1] Miloslav Nič, Jiří Jirát, Bedřich Košata, Aubrey Jenkins, and Alan McNaught, editors. *IUPAC Compendium of Chemical Terminology: Gold Book*. IUPAC, Research Triagle Park, NC, 2.1.0 edition, June 2009.

[2] Maria Flytzani-Stephanopoulos and Bruce C. Gates. Atomically Dispersed Supported Metal Catalysts. *Annual Review of Chemical and Biomolecular Engineering*, 3(1):545–574, 2012.

[3] Bruce C. Gates. Atomically Dispersed Supported Metal Catalysts: Seeing Is Believing. *Trends in Chemistry*, 1(1):99–110, April 2019.

[4] Gareth S. Parkinson. Single-Atom Catalysis: How Structure Influences Catalytic Performance. *Catalysis Letters*, 149(5):1137–1146, May 2019.

[5] Jingyue Liu. Catalysis by Supported Single Metal Atoms. *ACS Catalysis*, 7(1):34–59, January 2017.

[6] Huabin Zhang, Guigao Liu, Li Shi, and Jinhua Ye. Single-Atom Catalysts: Emerging Multifunctional Materials in Heterogeneous Catalysis. *Advanced Energy Materials*, 8(1):1701343, 2018.

[7] Botao Qiao, Aiqin Wang, Xiaofeng Yang, Lawrence F. Allard, Zheng Jiang, Yitao Cui, Jingyue Liu, Jun Li, and Tao Zhang. Single-atom catalysis of CO oxidation using Pt_1/FeO_x. *Nature Chemistry*, 3(8):634–641, August 2011.

[8] Xiao-Feng Yang, Aiqin Wang, Botao Qiao, Jun Li, Jingyue Liu, and Tao Zhang. Single-Atom Catalysts: A New Frontier in Heterogeneous Catalysis. *Accounts of Chemical Research*, 46(8):1740–1748, August 2013.

[9] Niancai Cheng, Lei Zhang, Kieran Doyle-Davis, and Xueliang Sun. Single-Atom Catalysts: From Design to Application. *Electrochemical Energy Reviews*, 2(4):539–573, December 2019.

[10] Chuan-Ming Wang, Yang-Dong Wang, Jun-Wei Ge, and Zai-Ku Xie. Reaction: Industrial Perspective on Single-Atom Catalysis. *Chem*, pages 2736–2737, November 2019.

[11] Charles T. Campbell and Zhongtian Mao. Chemical Potential of Metal Atoms in Supported Nanoparticles: Dependence upon Particle Size and Support. *ACS Catalysis*, 7(12):8460–8466, December 2017.

[12] Liangbing Wang, Wenbo Zhang, Shenpeng Wang, Zehua Gao, Zhiheng Luo, Xu Wang, Rui Zeng, Aowen Li, Hongliang Li, Menglin Wang, Xusheng Zheng, Junfa Zhu, Wenhua Zhang, Chao Ma, Rui Si, and Jie Zeng. Atomic-level insights in optimizing reaction paths for hydroformylation reaction over Rh/CoO single-atom catalyst. *Nature Communications*, 7:14036, December 2016.

[13] Suxia Liang, Ce Hao, and Yantao Shi. The Power of Single-Atom Catalysis. *ChemCatChem*, 7(17):2559–2567, 2015.

[14] U. Heiz, A. Sanchez, S. Abbet, and W.-D. Schneider. Catalytic Oxidation of Carbon Monoxide on Monodispersed Platinum Clusters: Each Atom Counts. *Journal of the American Chemical Society*, 121(13):3214–3217, April 1999.

[15] William E. Kaden, Tianpin Wu, William A. Kunkel, and Scott L. Anderson. Electronic Structure Controls Reactivity of Size-Selected Pd Clusters Adsorbed on TiO2 Surfaces. *Science*, 326(5954):826–829, November 2009.

[16] M. Valden, X. Lai, and D. W. Goodman. Onset of Catalytic Activity of Gold Clusters on Titania with the Appearance of Nonmetallic Properties. *Science*, 281(5383):1647–1650, September 1998.

[17] Jun Li, Xi Li, Hua-Jin Zhai, and Lai-Sheng Wang. Au20: A Tetrahedral Cluster. *Science*, 299(5608):864–867, February 2003.

[18] Robert Franke, Detlef Selent, and Armin Börner. Applied Hydroformylation. *Chemical Reviews*, 112(11):5675–5732, November 2012.

[19] Hans-Willi Bohnen and Boy Cornils. Hydroformylation of alkenes: An industrial view of the status and importance. In *Advances in Catalysis*, volume 47, pages 1–64. Elsevier, 2002.

[20] Florian P. Pruchnik. *Organometallic Chemistry of the Transition Elements*. Modern Inorganic Chemistry. Springer US, 1990.

[21] Matthias Beller, editor. *Catalytic Carbonylation Reactions*, volume 18 of *Topics in Organometallic Chemistry*. Springer Berlin Heidelberg, Berlin, Heidelberg, 2006.

[22] Majid Jahangiri, Richard T Jacobsen, Richard B. Stewart, and Robert D. McCarty. Thermodynamic Properties of Ethylene from the Freezing Line to 450 K at Pressures to 260 MPa. *Journal of Physical and Chemical Reference Data*, 15(2):593–734, April 1986.

[23] Gareth S. Parkinson. Iron oxide surfaces. *Surface Science Reports*, 71(1):272–365, March 2016.

[24] Pedro Tartaj, Maria P. Morales, Teresita Gonzalez-Carreño, Sabino Veintemillas-Verdaguer, and Carlos J. Serna. The Iron Oxides Strike Back: From Biomedical Applications to Energy Storage Devices and Photoelectrochemical Water Splitting. *Advanced Materials*, 23(44):5243–5249, November 2011.

[25] R Dictor. Fischer-Tropsch synthesis over reduced and unreduced iron oxide catalysts. *Journal of Catalysis*, 97(1):121–136, January 1986.

[26] Macarena Munoz, Zahara M. de Pedro, Jose A. Casas, and Juan J. Rodriguez. Preparation of magnetite-based catalysts and their application in heterogeneous Fenton oxidation – A review. *Applied Catalysis B: Environmental*, 176-177:249–265, October 2015.

[27] Werner Weiss and Wolfgang Ranke. Surface chemistry and catalysis on well-defined epitaxial iron-oxide layers. *Progress in Surface Science*, 70(1-3):1–151, March 2002.

[28] Minghui Zhu and Israel E. Wachs. Iron-Based Catalysts for the High-Temperature Water–Gas Shift (HT-WGS) Reaction: A Review. *ACS Catalysis*, 6(2):722–732, February 2016.

[29] R. Bliem, E. McDermott, P. Ferstl, M. Setvin, O. Gamba, J. Pavelec, M. A. Schneider, M. Schmid, U. Diebold, P. Blaha, L. Hammer, and G. S. Parkinson. Subsurface cation vacancy stabilization of the magnetite (001) surface. *Science*, 346(6214):1215–1218, December 2014.

[30] Roland Bliem. *Single metal adatoms at the reconstructed Fe_3O_4 (001) surface.* PhD thesis, Technical University of Vienna, Vienna, Austria, July 2016.

[31] Jan Hulva. *Studies of Adsorption on Magnetite (001) Using Molecular Beams.* Dissertation, Technical University of Vienna, Vienna, Austria, 2019.

[32] Michael Schmid. Experimentelle Methoden der Oberflächenphysik, 2018. Pages: 144.

[33] Jiri Pavelec, Jan Hulva, Daniel Halwidl, Roland Bliem, Oscar Gamba, Zdenek Jakub, Florian Brunbauer, Michael Schmid, Ulrike Diebold, and Gareth S. Parkinson. A multi-technique study of CO_2 adsorption on Fe_3o_4 magnetite. *The Journal of Chemical Physics*, 146(1):014701, January 2017.

[34] Daniel Halwidl. *Development of an Effusive Molecular Beam Apparatus*. Springer Fachmedien Wiesbaden, Wiesbaden, 2016.

[35] A. P. Grosvenor, B. A. Kobe, M. C. Biesinger, and N. S. McIntyre. Investigation of multiplet splitting of Fe 2p XPS spectra and bonding in iron compounds. *Surface and Interface Analysis*, 36(12):1564–1574, 2004.

[36] John F. Moulder, William F. Stickle, Peter E. Sobol, and Kenneth D. Bomben. *Handbook of X-ray Photoelectron Spectroscopy*. Perkin-Elmer Corporation Physical Electronics Division, 1992.

[37] A. Gedanken, N. A. Kuebler, and M. B. Robin. An MPI search for the $\pi \rightarrow 3\ p$ Rydberg states of ethylene. *The Journal of Chemical Physics*, 76(1):46–52, January 1982.

[38] D. G. Wilden and J. Comer. Rydberg states of $C_2h_4$and C_2d_4: assignments using the technique of low-energy electron energy-loss spectroscopy. *Journal of Physics B: Atomic and Molecular Physics*, 13(5):1009–1021, March 1980.

[39] Robert S. Mulliken. The excited states of ethylene. *The Journal of Chemical Physics*, 71(1):556–557, July 1979.

[40] Larry E. McMurchie and Ernest R. Davidson. Singlet Rydberg states of ethylene. *The Journal of Chemical Physics*, 67(12):5613–5618, December 1977.

[41] Ruth McDiarmid. A reinvestigation of the absorption spectrum of ethylene in the vacuum ultraviolet. *The Journal of Physical Chemistry*, 84(1):64–70, January 1980.

[42] K. E. Johnson, D. B. Johnston, and S. Lipsky. Electron impact spectra of some mono-olefinic hydrocarbonsa). *Journal of Chemical Physics*, 70(8):3844–3858, 1979.

[43] C. W. Bunn. The crystal structure of ethylene. *Transactions of the Faraday Society*, 40:23, 1944.

[44] G. J. H. Nes and A. Vos. Single-crystal structures and electron density distributions of ethane, ethylene and acetylene. III. Single-crystal X-ray structure determination of ethylene at 85 K. *Acta Crystallographica Section B Structural Crystallography and Crystal Chemistry*, 35(11):2593–2601, November 1979.

[45] Nassar Doudin, Simuck F. Yuk, Matthew D. Marcinkowski, Manh-Thuong Nguyen, Jin-Cheng Liu, Yang Wang, Zbynek Novotny, Bruce D. Kay, Jun Li, Vassiliki-Alexandra Glezakou, Gareth Parkinson, Roger Rousseau, and Zdenek Dohnálek. Understanding Heterolytic H_2 Cleavage and Water-Assisted Hydrogen Spillover on Fe_3O_4 (001)-Supported Single Palladium Atoms. *ACS Catalysis*, 9(9):7876–7887, September 2019.

[46] Martin Setvín, Margareta Wagner, Michael Schmid, Gareth S. Parkinson, and Ulrike Diebold. Surface point defects on bulk oxides: atomically-resolved scanning probe microscopy. *Chemical Society Reviews*, 46(7):1772–1784, April 2017. Publisher: The Royal Society of Chemistry.

[47] T Hanaoka, H Arakawa, T Matsuzaki, Y Sugi, K Kanno, and Y Abe. Ethylene hydroformylation and carbon monoxide hydrogenation over modified and unmodified silica supported rhodium catalysts. *Catalysis Today*, 58(4):271–280, May 2000.

[48] Long Chen, R. Scott Smith, Bruce D. Kay, and Zdenek Dohnálek. Adsorption of small hydrocarbons on rutile TiO_2(110). *Surface Science*, 650:83–92, August 2016.